USE OF INCIDENT AND REFLECTED SOLAR PARTICLE BEAMS TO TRACE THE TOPOLOGY OF MAGNETIC CLOUDS

Lun C. Tan[1,2], Olga E. Malandraki[2], Donald V. Reames[3], Chee K. Ng[4], Linghua Wang[5], and Gareth Dorrian[2]

[1] Department of Astronomy, University of Maryland, College Park, MD 20742, USA; ltan@umd.edu
[2] Institute of Astronomy and Astrophysics, National Observatory of Athens, Greece
[3] Institute for Physical Science and Technology, University of Maryland, College Park, MD 20742, USA
[4] College of Science, George Mason University, Fairfax, VA 22030, USA
[5] Space Science Laboratory, University of California, Berkeley, CA 94720, USA

ABSTRACT

Occasionally, large solar energetic particle (SEP) events occur inside magnetic clouds (MCs). In this work, the onset time analysis, the peak intensity analysis, and the decay phase analysis of SEPs are used to investigate two large SEP events inside MCs: the 1998 May 2 and 2002 April 21 events. The onset time analysis of non-relativistic electrons and $\sim$MeV nucleon^{-1} heavy ions shows the stability of the magnetic loop structure during a period of a few hours in the events examined. The joint analysis of pitch-angle distributions and peak intensities of electrons exhibits that, depending on the particle pitch angle observed at 1 AU, in the April event the reflection point of particles may be distributed along a wide spatial range, implying that the magnetic loop is a magnetic bottle connected to the Sun with both legs. In contrast, in the May event particle reflection occurs abruptly at the magnetic mirror formed by a compressed field enhancement behind the interplanetary shock, consistent with its open field line topology.

Key words: Sun: coronal mass ejections (CMEs) – Sun: heliosphere – Sun: magnetic topology – Sun: particle emission

Online-only material: color figures

1. INTRODUCTION

1.1. Significance of Examining Topology of Magnetic Clouds

The magnetic field topology in the inner heliosphere, i.e., the large-scale connection of the magnetic field lines that are driven by coronal eruption events into the interplanetary (IP) space (Kahler & Reames 1991), may bring important information on a variety of coronal processes. For example, approximately one-third of coronal mass ejections (CMEs) are well-organized magnetic clouds (MCs; Gosling 1990; Richardson & Cane 2010). The observed MC is characterized by a flux rope geometry in which the magnetic field lines are helically wound into a loop-like structure characteristic of a large, smooth rotation of the magnetic field, low proton temperature, and high field strength (Burlaga et al. 1981; Klein & Burlaga 1982). In addition, MCs are often associated with the bi-directional fluxes of suprathermal electrons (Gosling et al. 1987; Shodhan et al. 2000) and ions (Marsden et al. 1987) ejected from the solar corona. Gosling et al. (2001) observed the bi-directional suprathermal electron flux with roughly symmetrical 90° pitch-angle depression in the open field line topology, which is due to the adiabatic reflection at field enhancement beyond 1 AU. Also, Gosling et al. (2002) examined the bi-directional electron flux event in the closed field line topology, which is caused by the double magnetic connection to the Sun. Since the MC is the interplanetary manifestation of CME, it is important to trace its topology in order to understand the characteristics of coronal eruption processes.

1.2. Possible Topologies of Magnetic Clouds

According to Kahler & Reames (1991), there are three possible topologies of MCs.

1. *Magnetic "bottle."* Modeling efforts starting from Marubashi (1986) and Burlaga (1988) show that the MC could be a cylindrical magnetic flux rope with its two ends connecting back to the solar corona.
2. *Magnetic "bubble" or "plasmoid."* Piddington (1958) conjectured that the magnetic loop might be detached from the Sun to form a magnetic bubble. Also, Marsden et al. (1987) and Gosling et al. (1987) argued that their observations of bi-directional low-energy ion and electron fluxes, respectively, were more consistent with the explanation based on the detached bubble (plasmoid) topology of MCs.
3. *Open field line.* Azimuthal variation of solar wind speeds (Barouch & Burlaga 1976) or fast-mode shock waves (Parker 1958) may cause the field compression at the leading edge of MCs, because MCs travel faster than the ambient solar wind (Vandas et al. 2002; Mann 2006). As a result, a magnetic mirror could be formed behind the IP shock driven by an interplanetary CME (ICME).

It should be emphasized that the above classification of MC topologies is based on the assumed stability of the magnetic loop structure. In the two-component turbulence theory (Matthaeus et al. 1990), however, the observed particle motion is best modeled by the random walk of field lines in a two-dimensional (2D) magnetic turbulence that causes a fast diffusive separation of field lines at a distance greater than the parallel coherence length of $\sim$0.02 AU in the solar wind (Ruffolo et al. 2004). For the solar wind near 1 AU Matthaeus et al. (2010) further deduced a decorrelation time of $\sim$2.9 hr that measures the total contribution of turbulent fluid distortion factors, including rapid sweeping of the solar wind past the observer, nonlinear distortion, and wave propagation. Therefore, before examining the topology of MCs, we need to verify the stability of magnetic loops in the inner heliosphere. The onset time analysis of solar particles with different velocities may provide the evidence of

such stability, because along a stable loop structure the path length traveled by particles with different velocities from the Sun to the 1 AU observer should be nearly unchanged.

1.3. Use of Solar Energetic Particles to Trace the Topology of MCs

Since solar energetic particles (SEPs) accelerated in the parent flare or CME-driven shock wave can enter into the IP space through open field lines, quantitative examination of the intensity and anisotropy of SEPs is useful to distinguish among different magnetic topologies. The first attempt of using SEPs to trace the MC topology was made by Rao et al. (1967), who observed four intervals of bidirectional low-energy proton fluxes and explained their observation based on the open field line topology.

However, thus far, the cause of bi-directional low-energy particle flux has been unclear. The flux is present sporadically during the passage of an MC. In addition, bi-directional electron flux is not always coincident with bi-directional proton flux (Shodhan et al. 2000). Since the bi-directional particle flux has a long-lasting feature, it should be regarded as a "quasi-steady" phenomenon of MCs, as it cannot provide a "reference point" to signify the start of a physically interesting coronal process. However, the impulsive (Larson et al. 1997) and gradual (Malandraki et al. 2002) SEP events occurring inside MCs can provide such reference points to indicate the start of particle acceleration. For example, during an MC event occurring on 1995 October 18–20, Larson et al. (1997) observed five solar impulsive electron events indicating that at least one leg of the MC was magnetically connected to the Sun. The onset time analysis of these events shows that the path length traveled by electrons from the Sun to 1 AU varies from ∼3.2 AU near the MC exterior to ∼1.2 AU near the MC center, which is consistent with the force-free helical flux rope model of MCs. However, no more impulsive electron events with a path length of ⩾3.2 AU have been observed since Larson et al. (1997), even though an extensive search for such event in MCs (Kahler et al. 2011b) and ICMEs (Kahler et al. 2011a) has been completed.

Also, in previous studies only the onset time analysis of incident particle beams was used to determine the path length of SEPs traveling along one leg of MCs. Since we have established (Tan et al. 2009) the observational evidence indicating the presence of reflected particle beams in large SEP events, we are able to determine the path lengths of SEPs by using both incident and reflected particle beams. However, while the onset time analysis can estimate the path length traveled by particles from their reflecting point to the observer, it cannot determine the location of the reflecting boundary, which is dependent on the magnetic topology involved. Only the pitch-angle distribution (PAD) of particles may provide some hints on the property of magnetic topologies. For example, in the open field line topology particle reflection may occur abruptly at the magnetic mirror formed by a compressed field enhancement behind the IP shock. Because of a finite enhancement of the magnetic field strength at the magnetic mirroring point, a loss cone could appear in the PAD of reflected particles. In contrast, depending on the particle pitch angle observed at 1 AU, in the magnetic bottle topology the reflection point of particles may be distributed along a wide spatial range. Thus, the loss cone could be nearly absent because particle reflection occurs in the high field strength region close to the Sun. We will analyze the PAD information of particles to see whether we could find

the observational evidence of magnetic topology in the MC events examined.

1.4. Questions to Be Addressed in This Work

First, we will examine two representative SEP events, both of which occurred inside MCs during the solar cycle 23. The PAD information of non-relativistic electrons will be used to look for evidence of reflecting particle beams. The onset time analysis and peak intensity analysis of both incident and reflected particles will be used to determine the magnetic loop parameters during the onset phase and plateau phase, respectively. Comparing the loop parameters deduced in different phases, we are able to test the stability of the magnetic loop structure. Once the loop stability has been established, we will examine whether or not the magnetic loop forms a closed structure. Could the closed magnetic loop behave like a so-called particle "reservoir" (Roelof et al. 1992)? What are factors that affect the confinement of high-energy protons inside a reservoir?

In this work, we use the *Wind*/3-D Plasma and Energetic Particle Investigation (3DP; see Lin et al. 1995)/Semi-Conductor Detector Telescope (SST) and Electron Electrostatic Analyzer (EESA) electron data and the *Wind*/Energetic Particle Acceleration, Composition, and Transport Experiment (EPACT; see von Rosenvinge et al. 1995)/Low Energy Matrix Telescope (LEMT) heavy ion data. Also, we use the high-energy electron and proton data measured by the NOAA/*Geostationary Operational Environment Satellites* (*GOES*)/High Energy Proton and Electron Detector (http://spidr.ngdc.noaa.gov).

2. EVIDENCE OF PRESENCE OF REFLECTED PARTICLE BEAMS

2.1. Observed Data

For the *Wind*/3DP/SST electron data we have corrected for the ∼15% of incident electrons that scatter out of the silicon detector and leave only a fraction of their nominal energy in the detector, producing a spectrum that is approximately evenly distributed in energy below their nominal energy (Berger et al. 1969; Wang et al. 2011). The effect of the deposition energy correction is more significant during the onset phase of SEP events. Ignoring the correction may result in an unphysical path length (<1 AU) of incident electrons observed at 1 AU.

In this work we examine two large SEP events, which occurred inside MCs during the solar cycle 23: the 1998 May 2 and 2002 April 21 events. Previously Malandraki et al. (2002), Torsti et al. (2004), and Kocharov et al. (2007) examined the May event, during which the MC passed the *Wind* spacecraft between May 2 12:00 UT and May 3 17:00 UT (Richardson & Cane 2010). The parent (S18E20) flare and CME onset of the MC event occurred at April 29 15:57 UT and 16:22 UT, respectively. Also, the parent (S15W15) flare and CME onset of the SEP event occurred at May 2 13:26 UT and 13:29 UT, respectively. Note that hereafter the light-travel time of 8.3 minutes from the Sun to the Earth has been subtracted from the electromagnetic radiation observation time at 1 AU. In addition, Tylka et al. (2005, 2006) and Tan et al. (2008, 2009, 2011) examined the April event, during which the MC passed the *Wind* spacecraft between April 20 12:00 UT and April 21 18:00 UT. The parent (S14W34) flare and CME onset of the MC event occurred at April 17 07:42 UT and 07:52 UT, respectively. Also, the parent (S14W84) flare and CME onset of the SEP event occurred at April 21 00:51 UT and 01:08 UT, respectively. While the onset of the two SEP events examined was inside an MC, the onset

times in the May and April events were close to the start and center of the MC interval, respectively.

2.2. Pitch-angle Distribution of Solar Energetic Electrons

The most direct evidence of the presence of reflected electron beams can be seen from the pitch-angle spectrogram of solar electrons, which displays the temporal variation of their directional intensities as a function of the pitch-angle cosine (μ) of electrons. We prefer to use the spectrogram deduced from the *Wind*/3DP/SST electron data, because (1) the 3DP instrument has a $\sim 4\pi$ angular coverage, making it easy to detect both incident and reflected electron beams that are located along **B** or $-$**B** direction, where **B** is the magnetic field vector; (2) electrons detected by the SST sensor have higher velocity because of their energy coverage $E_e = 27$–300 keV (note that the velocity of 27 keV electrons is 2.3 AU hr^{-1}); (3) during the MC interval non-relativistic electrons detected by the SST sensor may experience scatter-free transport because of the diminished turbulence level in the solar wind (Tan et al. 2011).

The pitch-angle spectrogram of $\sim$66 keV SST electrons for the two events examined is shown in the upper panels of Figure 1, where electron data collected within each 5 minute interval are used to produce the spectrogram, and a high-order polynomial fitting is used to smooth data. The initial mass function (IMF) and solar wind data during the time period examined in Figure 1 are shown in Figure 2, from which it can be seen that the magnetic field strength B and the solar wind speed V_{sw} are quite stable during the event period. However, in the May event after the launch of the CME, **B** is deflected from the Parker spiral direction, as displayed in the left schematic of the center panel, where **B** is nearly sunward with a strong southward component, the incident and reflected particles are located in the $\mu < 0$ and $\mu > 0$ regions, respectively. In contrast, since in the April event **B** (see the schematic on the right) is nearly along the Parker spiral line, the incident and reflected particles are in the $\mu > 0$ and $\mu < 0$ regions, respectively.

In Figure 1, the presence of reflected particles is characterized by a counter-streaming electron beam with a deep depression at $\sim$90° pitch angles (see Tan et al. 2009), where the pitch-angle scattering alone is unlikely to produce a depletion of particles. Therefore, electron reflection is observed during >4 and >6 hr intervals in the May and April events, respectively.

2.3. Difference of Pitch-angle Distributions between 1998 May 2 and 2002 April 21 Events

While in the two events examined a counter-streaming electron beam with a deep depression at $\sim$90° of pitch angle is seen, the PAD details of reflected electrons are different. In fact, only in the first half hour since the appearance of reflected electrons are their PADs roughly similar in the two events examined. Later their PADs exhibit significant difference. In order to illustrate the difference, we present 10 minute cutoffs of electron pitch-angle spectrograms in the middle panels of Figure 1, where the directional electron intensity plotted has been subtracted off the background electron intensity. Since in the May event the background electron intensity exhibits temporal variation, a de-trend correction is carried out at each μ channel by linearly fitting the electron intensity data over an $\sim$1 hr time interval immediately before the event onset. In contrast, in the April event the mean intensity of background electrons is determined by averaging the electron intensity over an $\sim$1 hr period before the event onset.

In Figure 1 for each MC event, we show two cutoffs with the first one close to the onset of reflected electrons. The time difference between the two cutoffs is $\sim$40 minutes. It can be seen that in the May event the peak intensity of reflected electrons is located at $\mu_{po} \sim 0.7$–0.8 as observed at 1 AU. When $\mu \to 1$, the electron intensity decreases. At the event onset the intensity ratio $J(|\mu| = 0.97)/J(|\mu| = 0.83) = 0.67 \pm 0.05$, where $J(|\mu| = 0.97)$ (brown dots) and $J(|\mu| = 0.83)$ (green dots) are the electron intensities recorded in the sectors 1 and 2, respectively. As time passes the width of intensity peaks of reflected electrons gradually increases.

In contrast, in the April event reflected electrons are exhibited at $\mu < 0$. At the event onset the distribution of reflected electrons is roughly similar to that in the May event. However, after $\sim$1 hr since the event onset the observed electron intensity exhibits a continuous increase as $\mu \to -1$. The deduced intensity ratio $J(|\mu| = 0.97)/J(|\mu| = 0.83) = 2.2 \pm 0.4$, where $J(|\mu| = 0.97)$ (red dots) and $J(|\mu| = 0.83)$ (orange dots) are the electron intensities recorded in sectors 8 and 7, respectively. In addition, as time passes, the width of the intensity peak of reflected electrons at $\mu_{po} \sim -1$ gradually increases.

The ratio $J(|\mu| = 0.97)/J(|\mu| = 0.83)$ is related to the size of the loss cone (α_{loss}) at the magnetic mirroring point as observed at 1 AU. Note that the loss cone is a fundamental concept resulting from the conservation of the first adiabatic invariant,

$$\sin(\alpha_{loss}) = (B_{bkgd}/B_{max})^{1/2}, \qquad (1)$$

where B_{bkgd} and B_{max} are the background field strength and the maximum field strength at the magnetic mirroring point, respectively (see Bieber et al. 2002).

In order to explore how the $J(|\mu| = 0.97)/J(|\mu| = 0.83)$ ratio is related to α_{loss} observed at 1 AU, we need to understand the 3DP detector in some detail. As described in the Appendix, during the data reduction process of 3DP detectors the pitch-angle window with a width $\Delta\alpha = 22°.5$, which samples all angular bins inside a pitch angle sector, plays an important role in determining the angular response of a sector. The window effect is understandable by using a one-dimensional convolution as explained in the Appendix. Thus, for an assumed Gaussian distribution of detected electron intensities $J_e(\alpha, \alpha_0) \propto \exp(-\alpha^2/\alpha_0^2)$, where α_0 is the characteristic angular width of J_e, the electron intensity recorded in the Ith sector is

$$J I(\alpha_{loss}, \alpha_0) = \int_{\alpha_{loss}}^{\alpha_U} J_e(\alpha, \alpha_0)\varepsilon_I(\alpha)d\alpha, \qquad (2)$$

where α_U is the upper limit of integration and $\varepsilon_I(\alpha)d\alpha$ is the normalized solid angle element of the Ith sector. For sectors of $I = 1$ and 2 (or $I = 8$ and 7) $\varepsilon_I(\alpha)$ and $j_I = J_e(\alpha, \alpha_0)\varepsilon_I(\alpha)$ are shown later in Figure 15, from which $JII(\alpha_{loss}, \alpha_0)$ ($I = 1, 2$) can be calculated through numerical integration. For different α_0 values the $J1/J2$ (i.e., $J(|\mu| = 0.97)/J(|\mu| = 0.83)$) ratio thus deduced is plotted versus α_{loss} in the bottom panel of Figure 1, where the dot-dashed and dashed lines denote the observed $J(|\mu| = 0.97)/J(|\mu| = 0.83)$ levels in the May and April events, respectively. Note that for $\sim$66 keV electrons in the two MC events examined their α_0 range is between 30° and 40° (see the Appendix); we hence find $\alpha_{loss} = 19° \pm 5°$ and $3° \pm 3°$ in the May and April events, respectively, where the error of α_{loss} caused by the uncertainty of the angular bin size has been taken into account. Therefore, it appears that the loss cones are present and absent in the May and April events, respectively.
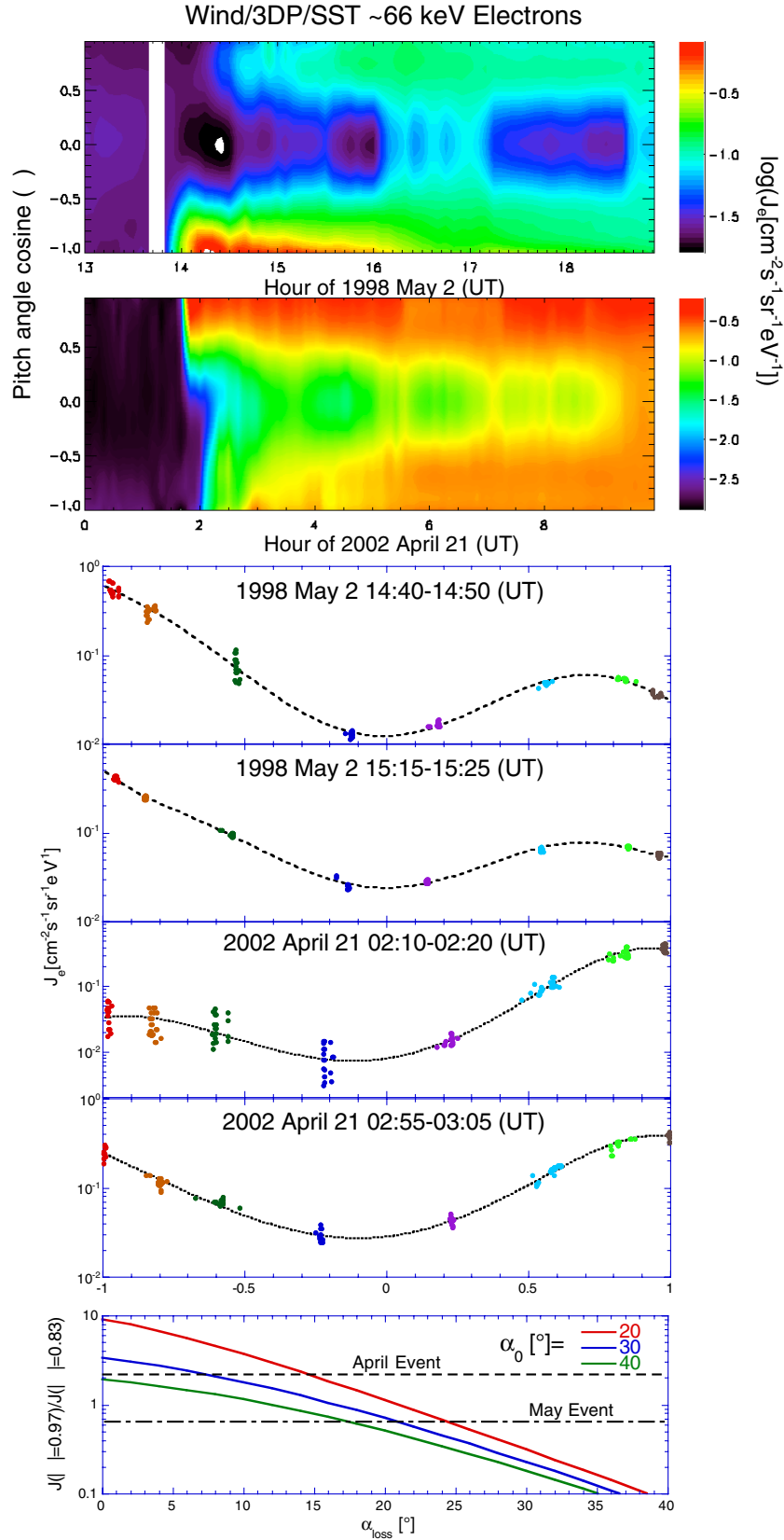
Figure 1. Upper: pitch-angle spectrograms of *Wind*/3DP/SST ~ 66 keV electrons are displayed with a 5 minute resolution. Because of the orientation difference of IMF (see Figure 2), reflected electrons are located at $\mu > 0$ and $\mu < 0$ regions in the 1998 May 2 and 2002 April 21 events, respectively. Lower: 10 minute cutoffs of spectrograms with background electron intensities subtracted are shown in the event onset. For each MC event we display two cutoffs with their time difference of ~ 40 minutes. Bottom: the simulated $J(|\mu| = 0.97)/J(|\mu| = 0.83))$ ratio is plotted vs. α_{loss} for different characteristic angular widths (α_0) of detected electron intensities.

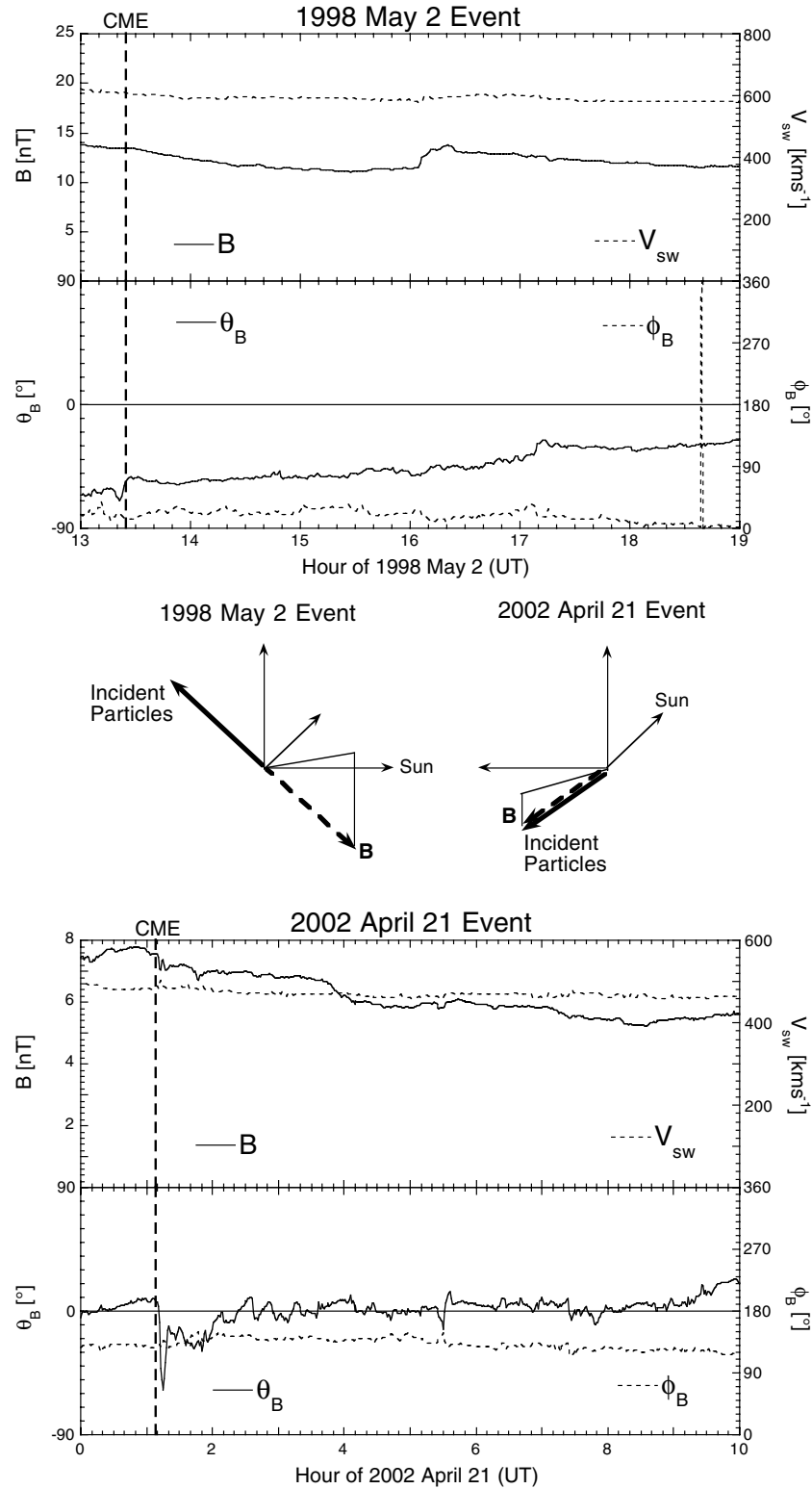(A color version of this figure is available in the online journal.)

Figure 2. IMF and solar wind data for the 1998 May 2 and 2002 April 21 events during the time intervals shown in the upper panels of Figure 1. The center panel denotes the **B** vector and the incident particle direction after the launch of CME in the two events examined.

Further, in the May event Skoug et al. (1999) observed an IP shock that occurred at 21:23 UT on 1998 May 1. The magnetic field compression behind the shock may result in the formation of a reflecting boundary for particles. However, from $\alpha_{loss} \leqslant 24°$ observed at 1 AU the predicated B_{max}/B_{bkgd} ratio is $\geqslant 6$ based on Equation (1), while the observed maximum enhancement

of the post-shock magnetic field strength (see Figure 6 in Malandraki et al. 2002) is $B_{max}/B_{bkgd} \sim 5$. Since α_{loss} observed at 1 AU is wider than that at the magnetic mirroring point (see Section 6.1), the divergence of B_{max}/B_{bkgd} between prediction and observation at the magnetic mirroring point should be even bigger. The divergence could be due to the residual scattering

of reflected electrons in the μ space, which would increase the $J(|\mu| = 0.97)/J(|\mu| = 0.83)$ ratio observed at 1 AU. In Section 6, we will explain why the PAD difference between the two events is useful in the examination of magnetic topologies.

3. ONSET TIME ANALYSIS OF SEPs

Assuming that the first arriving particles have experienced negligible scattering (Reames 2009), the solar release time (SRT, t_0) and the path length traveled by first arriving incident (L_{0i}) and reflected (L_{0r}) particles from their injection site near the Sun to the 1 AU observer can be deduced from the onset time analysis. The analysis identifies the loop parameters available at the onset phase of SEP events. Since it has been unclear so far whether the onset time of electrons is consistent with that of ions (Reames 2009), below we will estimate the onset time of both electrons and heavy ions separately.

3.1. 1998 May 2 Event

3.1.1. Observations

We demonstrate our technique by examining the May event, for which the onset time analysis was carried out by Malandraki et al. (2002) using the ACE/EPAM electron data and by Reames (2009) using the *Wind*/EPACT/LEMT heavy ion data. In the upper panels of Figure 3 we show the SST electron data in the May event. Since the peak of the reflected electron intensity does not appear at $\mu \sim 1$, in order to measure the times of the first arriving incident and reflected particles we have summed the particle directional intensity data into two hemispheres that distinguish between particles moving "along **B**" and "along **−B**" (Reames & Ng 2002), and correspond to "Reflected" and "Incident" electrons in the May event, respectively.

We follow Reames (2009) to calculate the relative intensity (RI) of electrons, i.e., the ratio of the measured intensity to the background intensity. Here a key factor is the choice of the interval used to estimate the background particle intensity. In view of the possible temporal variation of background intensities, the interval should be chosen as close as possible to the onset time of the event examined. In the case that the average background intensity varies with time, a de-trend correction is also necessary. We then estimate the standard deviation (σ) of RI in the background sampled interval, because the first detection of real signals is identified as a $>2\sigma$ increase over the preset background intensity level (Tylka et al. 2003, 2006). The vertical line in Figure 3 denotes the arrival time t_i of electrons thus deduced. Also, a similar analysis is carried out for the omnidirectional intensity data of LEMT He ions as shown in the bottom panel.

3.1.2. Analysis Results

For the May event the deduced t_i values of SST electrons and LEMT He ions are respectively plotted versus the reciprocal of particle velocity (v) in the upper and lower panels of Figure 4, into which the estimated t_0 and L_0 values are inserted. The t_0 value of incident electrons is consistent with that of reflected electrons. However, there is a $\sim$15 minute delay of incident He ions relative to electrons. Mewaldt et al. (2003) already noted that heavy ions are in general released later than electrons with a mean delay of 18 ± 16 minutes. On the other hand, the path length L_{0i} of incident electrons (1.15 ± 0.07 AU) is consistent with that of incident He ions (1.09 ± 0.04 AU) and
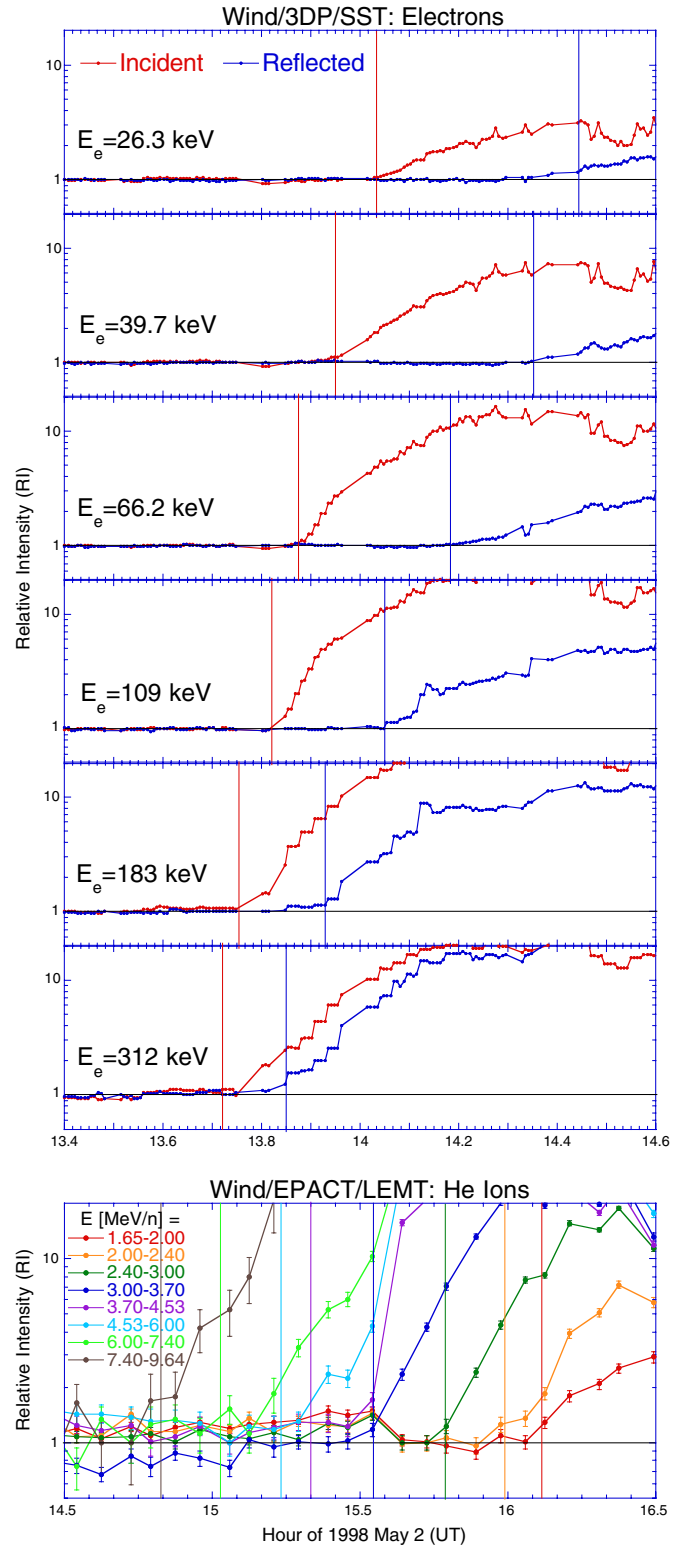

Figure 3. In the 1998 May 2 event, the time profiles of relative intensities of incident and reflected electrons measured by the *Wind*/3DP/SST sensor at different electron energies (E_e) are shown in the upper panels, where the incident and reflected electron data are taken from the "along −**B**" and "along **B**" hemispheres of PADs, respectively. The vertical red and blue lines denote the arrival times of incident and reflected electrons, respectively. Also, the time profiles of omnidirectional relative intensities of He ions as measured by the *Wind*/EPACT/LEMT sensor are shown in the bottom panel, where the vertical color lines denote the arrival times of incident He ions at different energies (E).

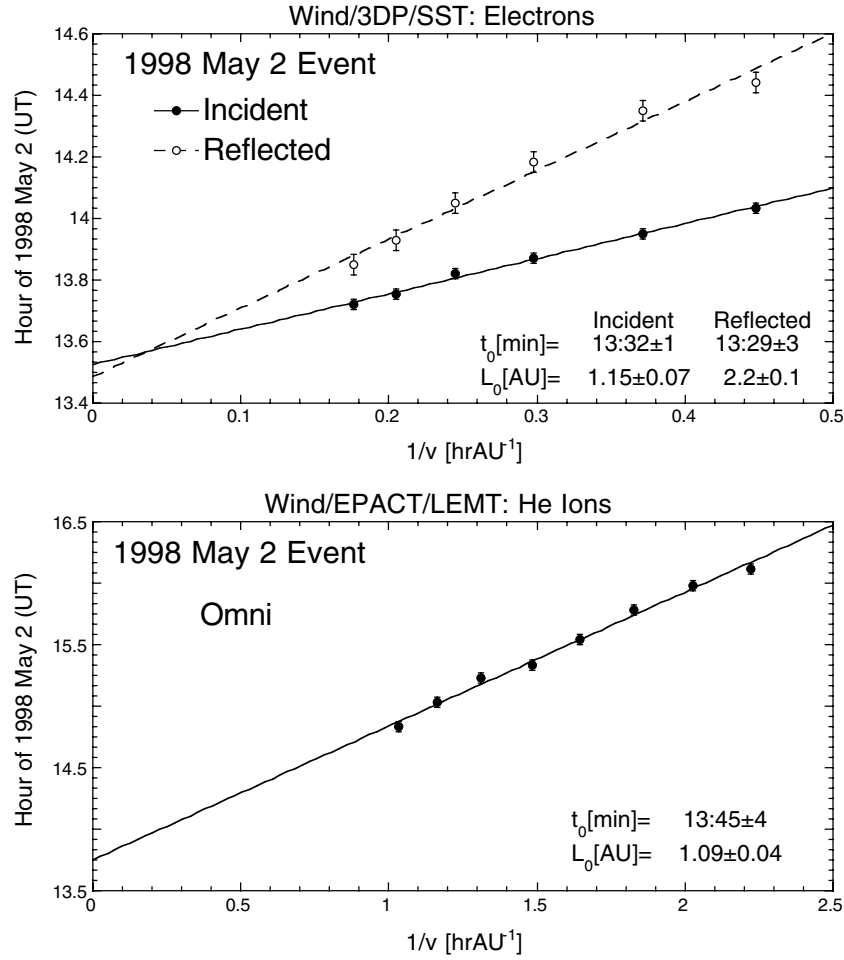(A color version of this figure is available in the online journal.)

Figure 4. In the 1998 May 2 event, the arrival times of electrons (upper panel) and He ions (lower panel) are plotted vs. $1/v$, where v is the particle velocity. The deduced SRT (t_0) and path length (L_0) are inserted into the figure.

Table 1
SRT and Path Lengths of Particles in the 1998 May 2 MC Event

	Time	3DP Electrons					LEMT Ions	
		t_{0i}	L_{0i}	t_{0r}	L_{0r}	l_{mo}[a]	t_{0i}	L_{0i}
	(UT)	(UT)	(AU)	(UT)	(AU)	(AU)	(UT)	(AU)
Flare (S15W15)	05/02 13:22							
Magnetic cloud	05/02 12–05/03 17							
CME	05/02 13:24							
Type III RB	05/02 13:27(DH)							
Type II RB	05/02 13:33(Metric)							
Electron onset	05/02 13:40–14:30	$13:32 \pm 1$	1.15 ± 0.07	$13:29 \pm 3$	2.2 ± 0.1	0.22 ± 0.07		
Ion onset	05/02 14:50–16:10						$13:45 \pm 4$	1.09 ± 0.04
Peak e intensity								
e PAD	05/02 13:50–14:30					0.15 ± 0.10		

Note. [a] l_{mo} is the projected on the ecliptic plane 2D path length of reflected particles traveling from their magnetic mirroring point (M) to the 1 AU observer (O).

also consistent with the length (1.06 AU) of the Parker spiral line under the observed solar wind speed (Malandraki et al. 2002). Since the arrival time of incident He ions is later than that of incident electrons (see Table 1), the consistency of L_{0i} between electrons and He ions implies that one leg of the MC, along which incident particles reach the 1 AU observer, is nearly unchanged during a ~2.5 hr period.

Also, Malandraki et al. (2002) estimated the path length (~0.23 AU) of reflected electrons from their magnetic mirroring point to the 1 AU observer, using the ACE/EPAM electron data at a single energy ($E_e = 112$–178 keV) channel. Since in the May event **B** has a strong southward component, as the averaged $\theta_B = -55° \pm 2°$ and $\phi_B = 24° \pm 4°$ during the one-hour period (13:30–14:30 hr UT, 1998 May 2; see Figure 2) after the CME onset, we ought to take the effect of θ_B into account. We hence distinguish between the projected on the ecliptic plane 2D path length l_{mo} of reflected electrons that travel from their magnetic mirroring point (M) to the 1 AU observer (O) and the

real path length $l_{mo}(\theta_B)$ that is deduced from the L_0 difference between incident and reflected electrons. From the observed L_0 difference we find $l_{mo}(\theta_B)/\mu_{po} = (L_{0r} - L_{0i})/2 = 0.54 \pm 0.08$ AU. Assuming that $\mu_{po} = 0.7 \pm 0.2$ (see Figure 1), we have $l_{mo}(\theta_B) = 0.38 \pm 0.12$ AU. In view of $\cos(\theta_B) = 0.57 \pm 0.02$ we finally obtain $l_{mo} = \cos(\theta_B)l_{mo}(\theta_B) = 0.22 \pm 0.07$ AU. Thus, the deduced radial component of l_{mo} is $\cos(\phi_B)l_{mo} = 0.20 \pm 0.06$ AU, which is consistent with the radial location ($r \sim 1.2$ AU) of the magnetic mirroring point identified by Malandraki et al. (2002).

3.2. 2002 April 21 Event

3.2.1. Observations

Since the background electron intensity in the April event is higher than that in the May event, care should be taken to identify the real arrival time of reflected electrons. In some cases (e.g., in the third panel of Figure 5) we may need to resolve the arrival time from a few candidates. In addition, the high background intensity may mask the real signal in the lowest E_e channel (see the top and second panels in Figure 5). In fact, Dalla et al. (2003) also noted that in large SEP events the velocity dispersion signal of low-energy electrons could be hidden by an incomplete correction of deposition-energy losses of high-energy electrons. We have hence ignored the $E_e = 27.7$ keV channel in the April event for further analysis.

3.2.2. Analysis Results

For the incident and reflected electrons in the April event our deduced t_0, L_{0i}, and L_{0r} values are given in the upper panel of Figure 6 (also see Table 2), from which it can be seen that both incident and reflected electrons have the same SRT.

Further, the L_{0i} value estimated from the April event shows interesting temporal variation. At the event onset $L_{0i} = 1.1 \pm 0.1$ AU deduced from the SST electron data is close to the length of the Parker spiral line, which explains why the velocity dispersion of energetic electrons in the April event is similar to that in the 1999 August 7 impulsive electron event (see Tan et al. 2011). However, $L_{0i} = 1.49 \pm 0.05$ AU deduced from LEMT He ion data is significantly greater than that from SST electron data. Since Figure 1 shows that in the April event the PAD of SST electrons at the event onset is different from that during the later time, the magnetic topology would experience temporal variation. Therefore, it is not surprising to see the temporal variation of deduced L_{0i} values. We will explain the stability of the magnetic loop structure during the later time in Section 4.3.

In Tylka et al. (2006), the SRTs of ACE/EPAM 175–312 keV electrons and GOES08 165–500 MeV protons are 01:23 UT and 01:31 UT, which are consistent with our deduced $01:21 \pm 2$ UT and $01:28 \pm 5$ UT of SST electrons and LEMT He ions, respectively.

In addition, from the deduced L_0 values we estimate the distance between the magnetic mirroring point and the 1 AU observer in the first hour from the event onset. Because $\theta_B \sim 0$ after the CME onset (see Figure 2), we approximate $l_{mo} = l_{mo}(\theta_B)$. The length of the flux tube l_{mo}, along which reflected particles from the magnetic mirror point travel back to 1 AU, is $l_{mo}/\mu_{po} = (L_{0r} - L_{0i})/2 = 0.24 \pm 0.08$ AU. Assuming that $\mu_{po} = 0.8 \pm 0.2$, we obtain $l_{mo} = 0.19 \pm 0.08$ AU. However, being different from the May event shown in Section 3.1.2, in the April event the *Wind* spacecraft failed to observe the magnetic field
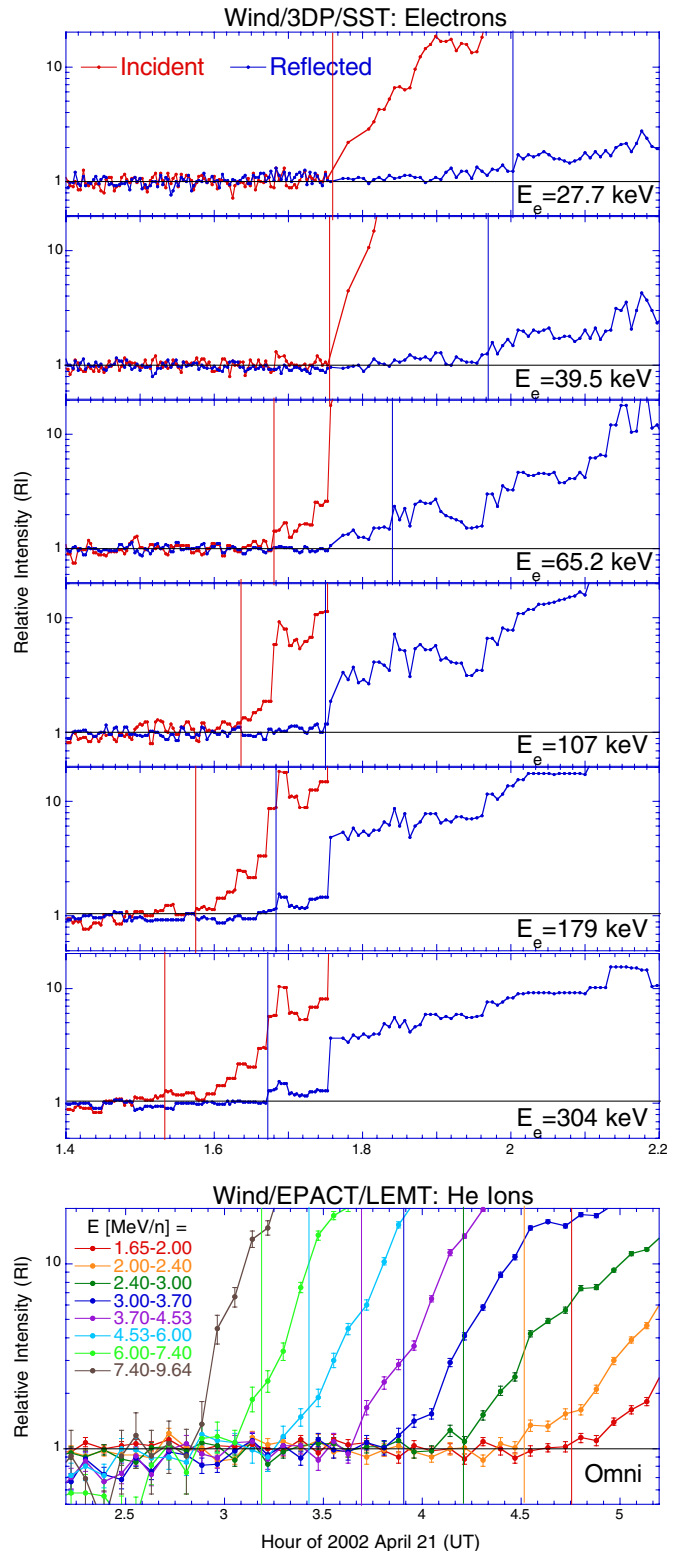

Figure 5. Same as Figure 3, but for the 2002 April 21 event, in which the incident and reflected electron data are taken from the "along **B**" and "along −**B**" hemispheres of PADs, respectively.

(A color version of this figure is available in the online journal.)

enhancement that caused the magnetic mirror. The enhancement might be wiped out because of a larger difference (89.3 hr) of onset times between the MC's CME and SEP's CME in the April event than that (69.1 hr) in the May event.
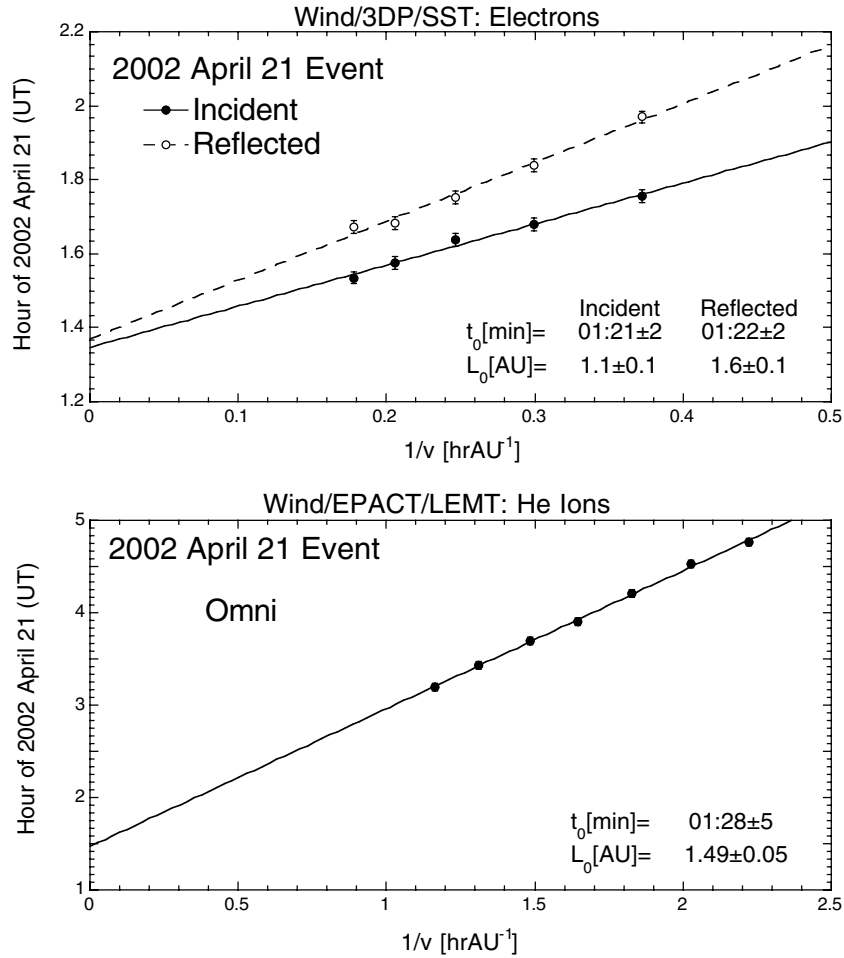
Figure 6. Same as Figure 4, but for the 2002 April 21 event.

Table 2
SRT and Path Lengths of Particles in the 2002 April 21 MC Event

	Time	3DP Electrons					LEMT Ions	
		t_{0i}	L_{0i}	t_{0r}	L_{0r}	l_{mo}	t_{0i}	L_{0i}
	(UT)	(UT)	(AU)	(UT)	(AU)	(AU)	(UT)	(AU)
Flare (S14W84)	04/21 00:51							
Magnetic cloud	04/20 12–04/21 18							
CME	04/21 01:09							
Type III RB	04/21 01:03(Metric)							
Type II RB	04/21 01:11(Metric)							
Electron onset	04/21 01:30–01:50	$01:21 \pm 2$	1.1 ± 0.1	$01:22 \pm 2$	1.6 ± 0.1	0.19 ± 0.08		
Ion onset	04/21 03:10–04:50						$01:28 \pm 5$	1.49 ± 0.05
Peak e intensity	04/21 02:00–07:00	$01:31 \pm 19$	1.6 ± 0.6	$01:43 \pm 29$	4.2 ± 1.2	1.3 ± 0.7[a]		
e PAD	04/21 01:50–03:00					1.47 ± 0.24[a]		

Note. [a] For $\mu \sim -1$ reflected electrons.

4. PEAK INTENSITY ANALYSIS OF SOLAR ELECTRONS

4.1. Comparison of Electron Observations by SST Sensor with That by EESA-H Sensor

As shown in Figure 1, in the April event only in the first hour from the event onset could the PAD of reflected electrons be similar to that in the May event; during the later time, the PAD of reflected electrons became narrower with the intensity peak at $\mu_{po} \rightarrow -1$, which is the focus of our further examination. Since the event development left the onset phase, we turn to the peak intensity analysis of solar electrons. Being different from

the onset time analysis in which the scatter-free transport of first arriving particles is generally acceptable (Reames 2009; Tan et al. 2011), electrons in their intensity peak need a longer time period to reach the 1 AU observer. Consequently, it is necessary to verify their scatter-free transport status during a longer period.

From the analysis of time profiles of 27–180 keV electrons in the 2002 October 20 solar impulsive electron event, Wang et al. (2011) identified the second intensity peak of inward-traveling electrons tens of minutes after the first peak, likely due to reflection/scattering at ~1.7 AU past the 1 AU observer. Following their approach, in the top panel of Figure 7 we plot
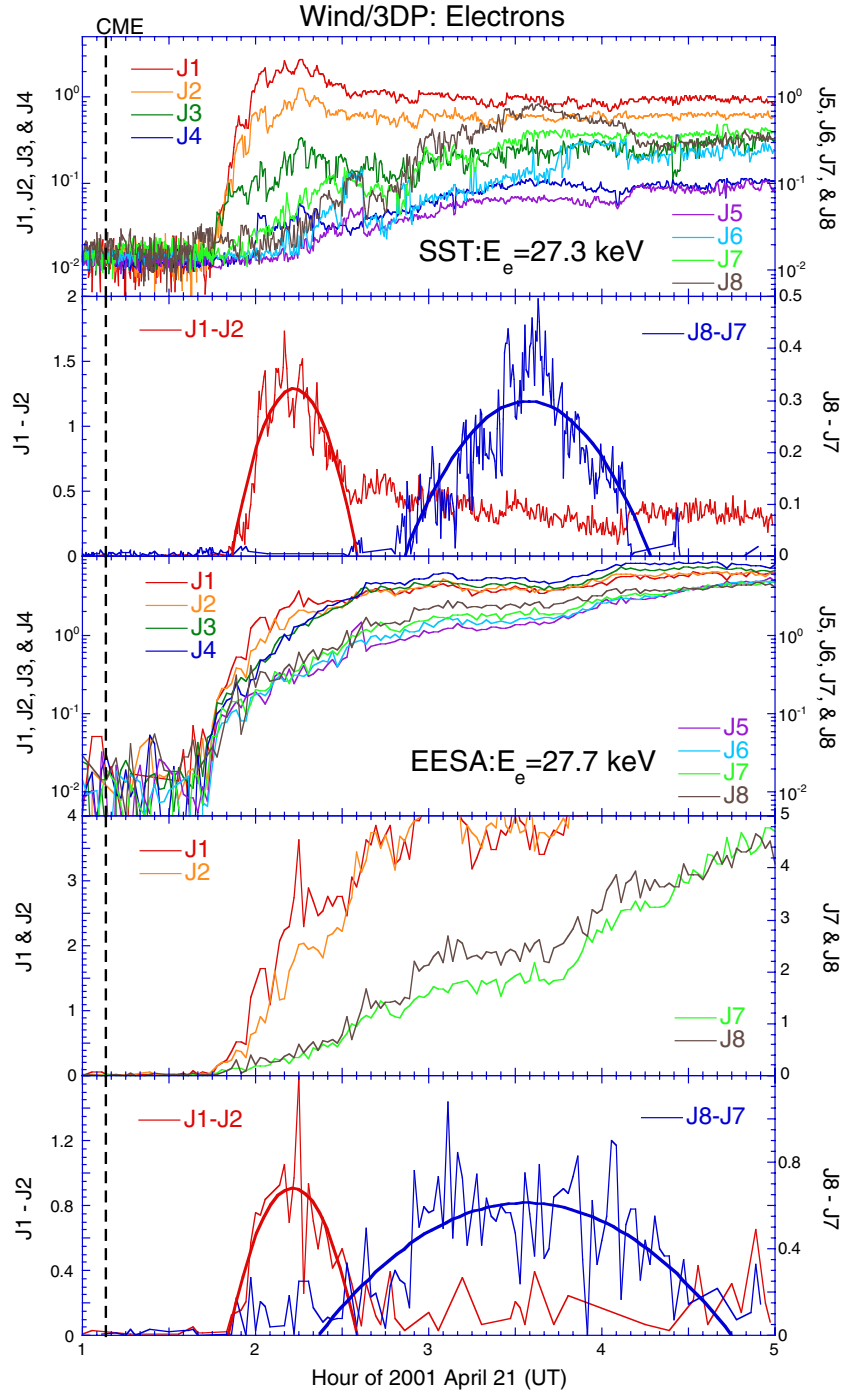
Figure 7. In the 2002 April 21 event, the time profiles of directional electron intensities at $E_e \sim 27$ keV as deduced from the SST (upper two panels) and EESA-H (lower three panels) sensors are shown. Here $J1, J2, \ldots, J8$ are the electron intensities recorded in different mean μ sectors (see the text), $J1$–$J2$ or $J8$–$J7$ is the difference of electron intensities recorded in two adjacent sectors, and the thick red and blue lines are the parabolic fitting results of $J1$–$J2$ and $J8$–$J7$, respectively. The electron intensity data in the fourth panel are in the linear scale.

(A color version of this figure is available in the online journal.)

the $E_e = 27.3$ keV directional electron intensity data measured by SST in the April event on a logarithmic scale. Here $J1, J2, \ldots$, and $J8$ are the electron intensities measured in sectors $1, 2, \ldots, 8$, whose average μ values are 0.97, 0.83, 0.55, 0.21, −0.21, −0.55, −0.83, and −0.97, respectively. It can be seen that along the anti-sunward direction ($J1$) we observe a broad intensity peak of outward-traveling electrons, while in the sunward direction ($J8$) we observe an even broader peak of inward-traveling electrons. The second peak was delayed by ∼1.5 hr relative to the first peak,

indicating that particle reflection also occurred at ∼1.7 AU past the observer at 1 AU.

In addition, in Tan et al. (2011) we analyzed the scatter-free transport condition of solar non-relativistic electrons. We observed the presence of an electron energy window, across which the scatter-free transport of lower energy electrons would change to the diffusive transport of higher energy electrons. In the April event, the transition energy is between 250 and 500 keV, below which incident electrons could reach the 1 AU

observer through scatter-free transport. However, in order to reach the 1 AU observer, reflected electrons need to travel a longer distance (>4 AU); they should experience even less scattering per unit path length. Consequently, their peaks are identifiable only in $E_e < 100$ keV, implying that only three lower energy channels of the SST sensor can be used in the peak intensity analysis. In order to improve the statistics, we need to use EESA-H electron channels at lower energies.

The highest energy channel of the EESA-H sensor is 27.7 keV, which is very close to the lowest energy channel (27.3 keV) of the SST sensor. Therefore, similar to the SST plot in the top panel of Figure 7, we show the EESA-H plot at $E_e = 27.7$ keV in the third panel, where no clear intensity peak is seen. The absence of intensity peaks is due to the instrumental noise that mainly appears in the 4–27 keV range of the EESA-H sensor (see Wang et al. 2006). While the noise smears the intensity peak of recorded electrons, reflected electrons are still detectable. This point can be seen from the time profiles of electron intensities in a linear-scale plot as shown in the fourth panel, where excess counts appear in 1 and 8 sectors above the instrumental background estimated from 2 and 7 sectors, respectively. The center of excess counts is located at the electron intensity peak observed by the SST sensor (see the top panel), indicating the real existence of incident and reflected electrons in the EESA-H data.

4.2. Measurement of Electron Intensity Difference between Adjacent Channels

As explained in the Appendix, we have found that the detection of electron intensity difference between two adjacent sectors (e.g., $J1$–$J2$ or $J8$–$J7$) can reduce the instrumental background but not hurt the real signal. Therefore, the intensity difference output ($J1$–$J2$ or $J8$–$J7$) is used as a new "channel" to detect the narrow beam of electrons that may be reflected back from the vicinity of the Sun.

Here we show the result of intensity difference calculations for ∼27 keV electrons detected by SST and EESA-H in the second and bottom panels of Figure 7, respectively. It can be seen that the instrumental background in the EESA-H data is more serious than that in the SST data. Nevertheless, the output of $J8$–$J7$ from EESA-H exhibits a real peak of reflected electrons. In Figure 7, the red and blue thick lines are the parabolic fitting results of incident and reflected electron intensity peaks, respectively, which can be used to determine the location and FWHM of electron intensity peaks. By comparing the second panel with the bottom panel, we find that the deviations of peak arrival times between SST and EESA-H are only 0.50 and 0.76 minutes for incident and reflected electrons, respectively. Therefore, according to our "calibration" procedure we have not found any significant deviation of electron peak arrival times between SST and EESA, making it easy to carry out a combination analysis of both SST and EESA-H data.

4.3. Analysis Result

For the April event we show all peak electron intensity data collected from both SST and EESA-H sensors in Figure 8, where the red and blue thick lines are the parabolic fitting results of incident and reflected electron intensity peaks, respectively. The fitting is generally acceptable, except for the reflected electrons at the $E_e = 8.88$ keV channel, where an oversubtraction might happen in the center of the reflected electron peak.

The arrival time of peak electron intensities in the April event is plotted versus $1/v$ of electrons in Figure 9, where the standard deviation (σ) of the arrival time of peak electron intensities is taken to be the FWHM/2 value of the fitted electron intensity peak. In addition, the nominal electron energy is taken to be the mean value of the sampled energy interval. From the figure it can be seen that the SRT of reflected electrons is consistent with that of incident electrons. In addition, since the observed interval of LEMT He ion onset is within that of SST peak electron intensities (see Table 2), the consistency of the L_{0i} value deduced from the onset time analysis of He ions ($L_{0i} = 1.49 \pm 0.05$ AU) with that from the peak intensity analysis of electrons ($L_{0i} = 1.6 \pm 0.6$ AU) is in support of the stability of magnetic flux tubes during a ∼5 hr interval in the later time (02:00–07:00 UT, 2002 April 21, see Table 2) in the April event.

Furthermore, from the path length difference between reflected and incident electron peaks we estimate that the length of the flux tube, along which the $\mu_o \sim -1$ reflected particles as observed at 1 AU could reach their reflecting point, is $l_{mo} = 1.3 \pm 0.7$ AU, which is close to the length of the Parker spiral line. Thus, the observed reflected electrons at $\mu_o \sim -1$ could reach the vicinity of the Sun, implying a magnetic bottle topology involved in the April event (see Section 6). In contrast, there is no velocity-dispersed intensity peak of reflected electrons exhibited at $\mu_o \sim 0.7$–0.8 in the May event, which is consistent with its open field line topology (also see Section 6).

5. DECAY PHASE ANALYSIS OF SEPs

5.1. Duration Enhancement of High-energy Particle Intensities

Because of the existence of reflecting boundaries of SEPs, near 1 AU the observed SEP event could be additionally amplified, causing the so-called reservoir effect (Roelof et al. 1992). The effect makes the intensity-time profile of high-energy particles more prolonged than would be expected based on the assumption of SEP transport in the standard solar wind (Tan et al. 2008, 2009; Reames 2010). While traditionally (e.g., Roelof et al. 1992) the reservoir effect is referred to the very low energy particles that have reached the same intensities and spectra over widely separated regions, what we are concerned with is the effect of high-energy protons because of its impact on the space weather issue. It is interesting to examine the spatial and temporal variation of high-energy proton intensities in the inner heliosphere. Through the analysis of particle confinement mechanisms occurring in individual flux tubes we are able to understand the conditions that enhance the duration of high-energy proton intensities in different magnetic field topologies.

In fact, among various SEPs high-energy protons represent "hard" radiation that can be a significant hazard to astronauts and equipment in space, while secondary neutrons threaten passengers and crew of aircraft on polar routes. Taking into account typical proton energy spectra and the thickness of available shielding, the most important energy range for protons is from 30 to 100–200 MeV (Turner 2006).

It is known (Reames et al. 1996; Lee 2005) that even in a completely closed magnetic flux tube the time profile of high-energy proton intensities eventually would undergo an exponential decay because of the expansion of their occupied volume with the solar wind, which causes the adiabatic deceleration of particles. That explains why in the two MC events examined the high-energy particle intensity eventually displays an exponential decay with the characteristic decay time τ_d. Recently, Lario (2010) analyzed the dependence of τ_d on various factors,
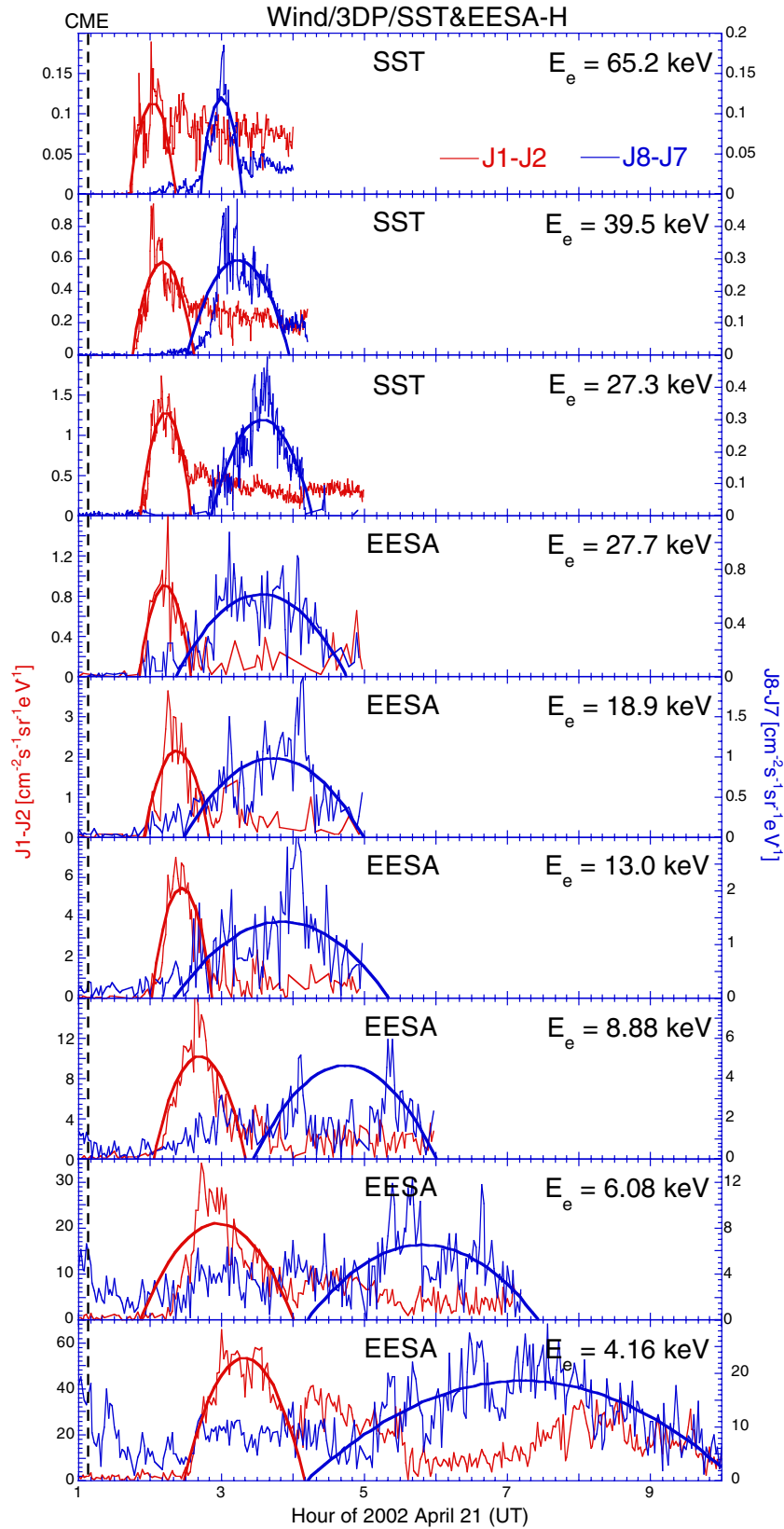
Figure 8. In the 2002 April 21 event, the time profiles of peak intensities of incident and reflected electrons as deduced from SST and EESA-H are shown. The red and blue lines are the parabolic fitting results of incident and reflected electron intensities, respectively.

(A color version of this figure is available in the online journal.)

including electron energy spectrum, solar wind velocity, and observer position relative to the parent flare. No significant dependence of τ_d on these factors has been found.

We have noted that the two SEP events examined have different PADs. In the May event the presence of a loss cone in the PAD indicates that the magnetic mirror only reflects SEPs
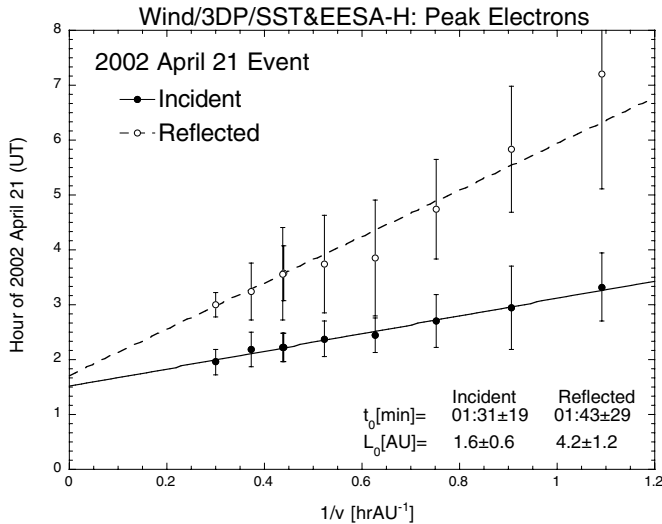
Figure 9. Peak electron arrival times as measured by both SST and EESA-H are plotted vs. $1/v$ in the 2002 April 21 event. The deduced values of SRT (t_0) and path length (L_0) are inserted into the figure.

outside the loss cone back to 1 AU, whereas SEPs inside the loss cone would be lost during their further transport process. On the contrary, in the April event with $\mu_{loss} \rightarrow -1$ almost all particles could be reflected back to 1 AU. Therefore, we should expect a smaller τ_d value in the May event, because the additional loss of high-energy particles inside the loss cone would result in a faster decay of particle intensities. Our expectation is consistent with the GOES08 observations given in Figure 10, where the high-energy electron and proton data in the May and April events are shown in the upper and lower panels, respectively. Note that two vertical dashed lines limit the exponential decay interval of high-energy particle intensities, which occurred after half a day and one day from the event onset in the May and April events, respectively. The τ_d value of high-energy protons in the April event is ~1.4 times greater than that in the May event.

It is noticeable that in the May event the sampled interval of τ_d is mostly inside the MC, whereas in the April event it is outside the MC. However, we have not taken the position difference of sampled intervals relative to MC into account. It is because the τ_d value of high-energy protons is mainly dependent on the degree to which the field lines are closed in magnetic flux tubes according to the simulation of Kocharov et al. (2009). However, a magnetic tube located inside an MC does not enhance the fraction of its closed field lines, because the MC itself may not be a closed field structure. Recent anomalous cosmic ray observations (Reames et al. 2009) cast doubt on conventional ideas about the closed field topologies of MCs. In fact, in order to explain the simultaneous observation of anomalous cosmic rays from the outer heliosphere and counter-streaming suprathermal electrons from the corona, Reames (2010) assumed that the field lines that are open to the outer heliosphere must be mixed with closed field lines on a fine spatial scale. Therefore, the position of sampled magnetic tubes relative to an MC may affect τ_d less.

6. DISCUSSIONS

It is generally accepted that particle reflection is a magnetic phenomenon occurring in the space plasma. While the onset time analysis can estimate the path length traveled by reflected particles from their reflecting point to the observer, single spacecraft measurement cannot identify the location of the

reflecting boundary. Nevertheless, since we have observed the PAD difference of non-relativistic electrons between the two MC events examined (see Figure 1), we wish to use the PAD information to infer the property of the reflecting boundary. For example, does particle reflection occur abruptly or is it distributed over a wide spatial range? In order to answer this question, we need (1) to build a model (schematic) to approximate the particle transport in the MC event examined, (2) to determine the model parameter range by comparing the model prediction with observations, and (3) to infer the IMF topology from the model parameters constrained by observations. Below we will examine the two MC events separately.

6.1. IMF Topology at the Onset of the 1998 May 2 Event

We show the diagrams that schematically describe different magnetic field topologies in Figure 11, where the field lines illustrated are located in the area accessible to incident particles. The schematic that describes the magnetic topology in the May event is similar to the "open field line" topology in Kahler & Reames (1991, see their Figure 1). As shown in the left panel of Figure 11, the incident particles (the red dashed line) come from their acceleration site near the Sun, while the reflected particles (the purple dashed line) originate from the magnetic mirror formed by the compressed field enhancement behind an IP shock (the green dashed line) that is driven by a CME. Along the field line the path length of reflected particles from the magnetic mirroring point (M) to the 1 AU observer (O) is l_{mo}. Because of a limited enhancement of the magnetic field strength, we ought to expect a loss cone with finite size. Outside the loss cone ($\mu < \mu_{loss}$) particles should be abruptly reflected back to 1 AU, while inside the loss cone ($\mu > \mu_{loss}$) particles could escape along the open field line.

Parker (1958) modeled the configuration of a steady-state IMF resulting from the spherically symmetric solar wind ejected from a rotating Sun. In a "zero-order" approximation near the solar ecliptic plane (Klein et al. 1987) his model predicts that $B_\phi = B_0/r$ and

$$B_\rho = B_0(1 + r^2)^{1/2}/r^2, \qquad (3)$$

where B_ϕ and B_ρ are the azimuthal and radial component of **B**, respectively. By examining the IMF data measured by the *Voyager* spacecraft within $r = 1$–20 AU, Klein et al. (1987) found that the average field strength B also satisfies Equation (3) with $B_0 = 4.9$ nT. Therefore, from the equation we have $B \propto r^{-2}$ at $r \ll 1$ AU and $B \propto r^{-1}$ at $r \gg 1$ AU. In addition, from the conservation of the first adiabatic invariant we have

$$B/\sin^2\alpha = B/(1 - \mu^2) = \text{Const}. \qquad (4)$$

For the magnetic mirror point located at M, where the background field strength is B_m (regardless of the enhanced field strength (B_{max}) due to the presence of the magnetic mirror), the reflected particles with the initial $\mu = \mu_m$ would have $\mu = \mu_o$ observed at 1 AU,

$$\mu_o = (1 - (1 - \mu_m^2)B_o/B_m)^{1/2}. \qquad (5)$$

Assuming that in the μ range concerned by us the interplanetary transport process does not alter the PAD of reflected particles significantly, under the scatter-free transport assumption the observation time t_o of first reflected particles arriving at 1 AU is

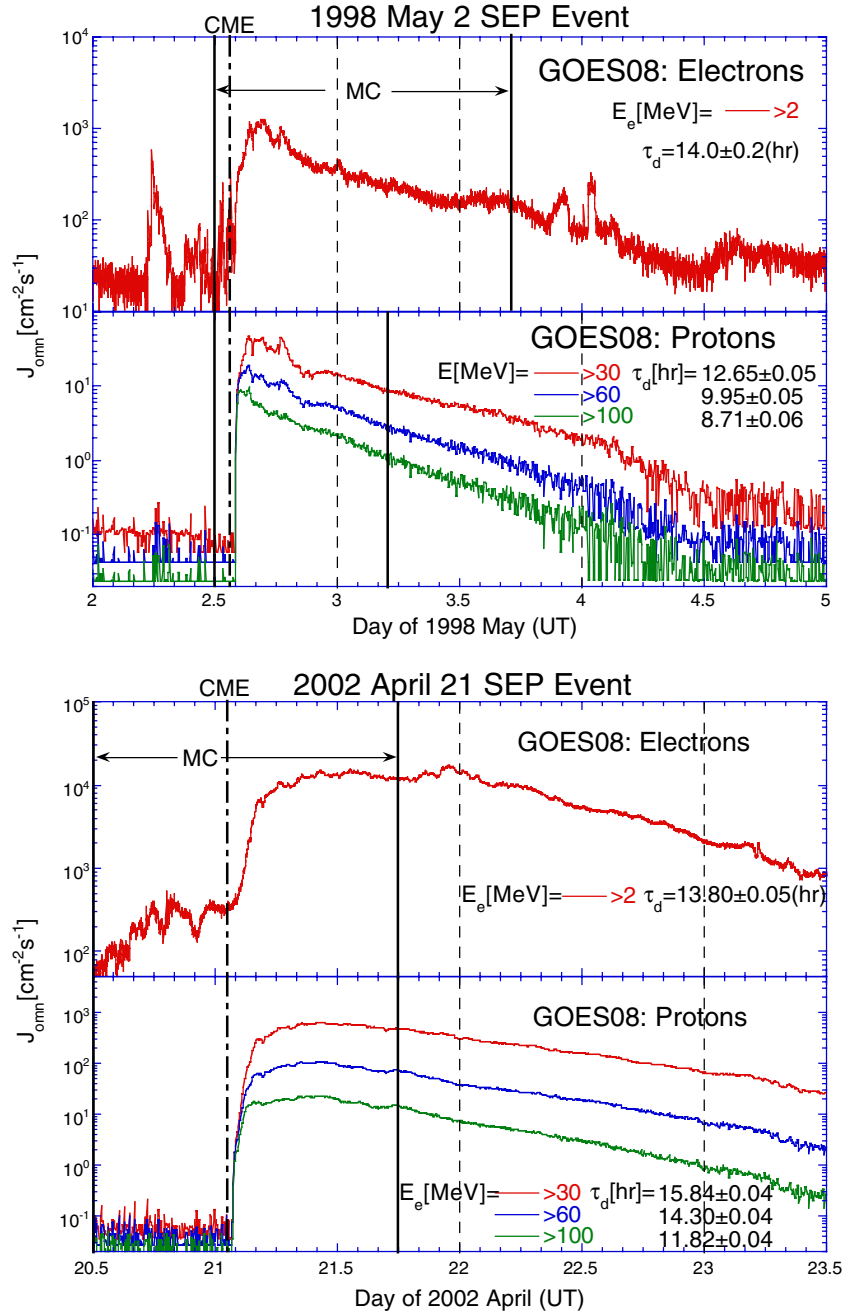$$t_o = t_m + l_{mo}(\theta_B)/(\mu_o v), \qquad (6)$$

Figure 10. Time profiles of omnidirectional high-energy electron and proton intensities as measured by GOES08 are shown in the upper and lower panels for the 1998 May 2 and 2002 April 21 events, respectively. The two vertical dashed lines limit the sampled exponentially decay interval of high-energy particle intensities.

(A color version of this figure is available in the online journal.)

where v is the particle speed and t_m is the time at which reflected particles first left the magnetic mirror.

Here we examine the μ_m range in which the relative difference between $1/\mu_o$ and $1/\mu_m$ is smaller, so in Equation (6) the variation of $1/\mu$ along the path length $l_{mo}(\theta_B)$ of reflected particles could be ignored. We hence plot the relative difference $\delta\mu = (1/\mu_o - 1/\mu_m)/(1/\mu_m)$ deduced from Equations (3) and (5) versus μ_m in the bottom panel of Figure 12. It can be seen that at $r_m \leqslant 1.2$ AU $\delta\mu < 10\%$ in the higher μ_m sectors (sectors 1–2 and 7–8). However, $\delta\mu$ quickly increases as μ_m decreases. In the $\mu_m \sim 0.6$ sectors (sectors 3 and 6), $\delta\mu \sim 50\%$, indicating that along $l_{mo}(\theta_B)$ the relative deviation of $1/\mu$ from its average reaches $\delta\mu/2 = 25\%$. Obviously, data in the $\mu_m \sim 0.2$ sectors (sectors 4 and 5) cannot be used in Equation (6).

In fact, in the May event only at three lower energy channels of the 3DP/SST sensor can the velocity-dispersed arriving time of reflected electrons in sectors 1–3 and 6–8 be identified. Here we show the time profiles of directional electron intensities in the matched incident and reflected μ sectors (i.e., with same $|\mu|$ value) at the lowest energy channel ($E_e = 26.3$ keV) of SST in the upper panels of Figure 12, where a high and varying background intensity of electrons is visible. Nevertheless, we can identify the onset time t_o (the vertical color line) of both incident and reflected electrons by referring the abrupt increase of electron intensities relative to their average background level (the dotted line) with a time resolution of ± 5 minutes.

The t_o values deduced from three lower energy channels of the 3DP/SST sensor are plotted versus $1/\mu_o v$ in the top panel
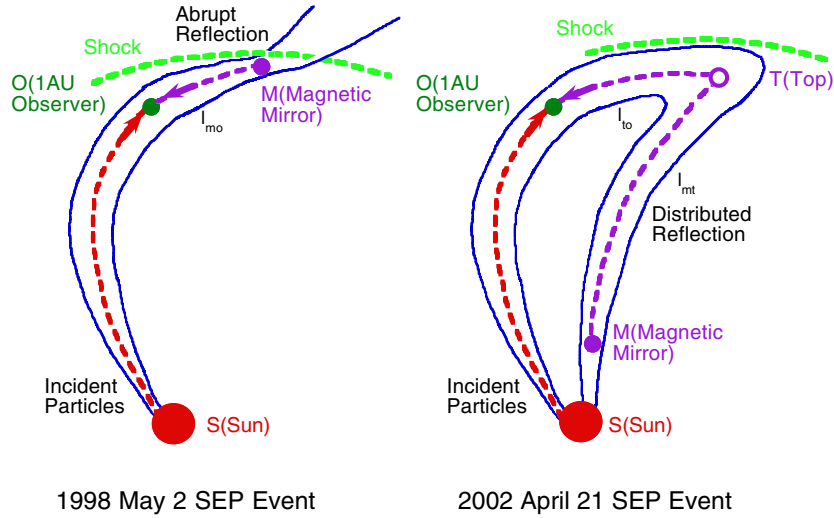
14

Figure 11. Schematics to show the 2D magnetic field topologies suggested for the 1998 May 2 and 2002 April 21 events. In the May event (left panel), l_{mo} is the path length traveled by reflected particles from the magnetic mirroring point (M) to the 1 AU observer (O). In the April event (right panel), $l_{mo} = l_{mt} + l_{to}$, and the field line between the Sun (S) and a top point (T) can be approximated by a Parker spiral.

(A color version of this figure is available in the online journal.)

of Figure 13, from which we obtain $t_m = 14.08 \pm 0.09$ hr (UT) and $l_{mo}(\theta_B) = 0.27 \pm 0.17$ AU. Relative to the time at which incident electrons with ~ 40 keV energy (i.e., the mean energy of three lower energy channels in the SST sensor) reach half of their peak intensity (Figure 3), the delay of t_m is ~ 0.1 hr, which is the time interval required by incident electrons with $\mu \sim 0.7$–0.8 for traveling from 1 AU to the magnetic mirroring point. Also, from the deduced $l_{mo}(\theta_B)$ value we estimate (see Section 3.1.2) $l_{mo} = 0.15 \pm 0.10$ AU, which is consistent with l_{mo} deduced from the path length difference between incident and reflected electrons (see Table 1).

It is also interesting to plot t_o data of the April event, where the procedure to identify the t_o value is illustrated in Figure 14, in which electron data at the lowest energy channel of SST ($E_e = 27.7$ keV) are shown. Note that around 02:35 UT during the time interval limited by the two vertical dashed lines the interference of non-velocity-dispersed electrons appears in all μ sectors of reflected electrons. Nevertheless, the onset time of reflected electrons can be determined from the start time of a continuous intensity enhancement of reflected electrons until reaching their peak, regardless of the contribution of interfering electrons. The t_o data thus deduced from sectors 1–3 and 6–8 are shown in the second panel of Figure 13, from which the deduced l_{mo} value is negative, indicating that the April event cannot be explained by using Equation (6). In fact, the negative l_{mo} value is due to an earlier arrival of lower μ_o electrons, which is more consistent with a distributed particle reflection as shown in the right panel of Figure 11.

6.2. IMF Topology in the 2002 April 21 Event after One Hour from the Event Onset

As shown in the sixth panel of Figure 1, in the April event after one hour from the event onset (i.e., after ~ 30 minutes since the appearance of reflected electrons) the loss cone in the PAD of non-relativistic electrons is nearly absent, indicating that B_{max} at the magnetic mirroring point is almost "infinite." This could occur when the reflecting point is near the Sun, where the field strength is very large when compared with the 1 AU observed value. We hence speculate that, depending on the μ_o value observed at 1 AU, the particle reflection point in the April

event may be along a flux tube shown in the right panel of Figure 11. Thus, we assume that the magnetic field topology is a magnetic loop comprising a propagating arch connecting two legs of the Parker spirals (Kocharov et al. 2007).

Further, we assume that the field line between the Sun (S) and a top point (T) can be approximated by a Parker spiral line, while the field line from T to O is similar to that from M to O in the left panel. Therefore, similar to the left panel, we also have $\mu_t \sim \mu_o$ (see Section 6.1). Further, assuming that the magnetic mirroring point M is located at some place between S and T along the Parker spiral line, we can calculate the time interval Δt by which reflected particles starting from M reach O,

$$\Delta t = t_{mt} + t_{to} \sim \int_{r_m}^{r_t} dl/(\mu v) + l_{to}/(\mu_o v), \qquad (7)$$

where t_{mt} and t_{to} are the time intervals during which electrons travel between M–T and T–O, respectively. Observationally, Δt is half of the t_o difference between the matched incident and reflected μ channels. Since the integral

$$\int_{r_m}^{r_t} dl/(\mu v) = \int_{r_m}^{r_t} dr/(\mu v \cos(\theta_{sB})), \qquad (8)$$

where the angle between the solar wind direction and **B**, θ_{sB} satisfies the relation that

$$\tan \theta_{sB} = \Omega_s r / V_{sw}, \qquad (9)$$

where Ω_s is the solar sideral rotation rate. With $V_{sw} \sim 500$ km s^{-1} in the April event, from Equation (9) the largest $\theta_{sB} = 41°$ (cos $\theta_{sB} = 0.76$) at $r \sim 1$ AU and the smallest $\theta_{sB} = 0°$ (cos $\theta_{sB} = 1$) at $r \sim 0$ AU. Therefore, within our concerned r range the factor cos θ_{sB} is close to a constant $\langle \cos\theta_{sB} \rangle = 0.88 \pm 0.12$. Consequently,

$$\int_{r_m}^{r_t} dl/\mu v \sim (v \langle \cos(\theta_{sB}) \rangle)^{-1} \int_{r_m}^{r_t} dr/\mu. \qquad (10)$$

Assuming that the magnetic field strength $B \propto r^{-2}$, from the conservation of the first adiabatic invariant we have

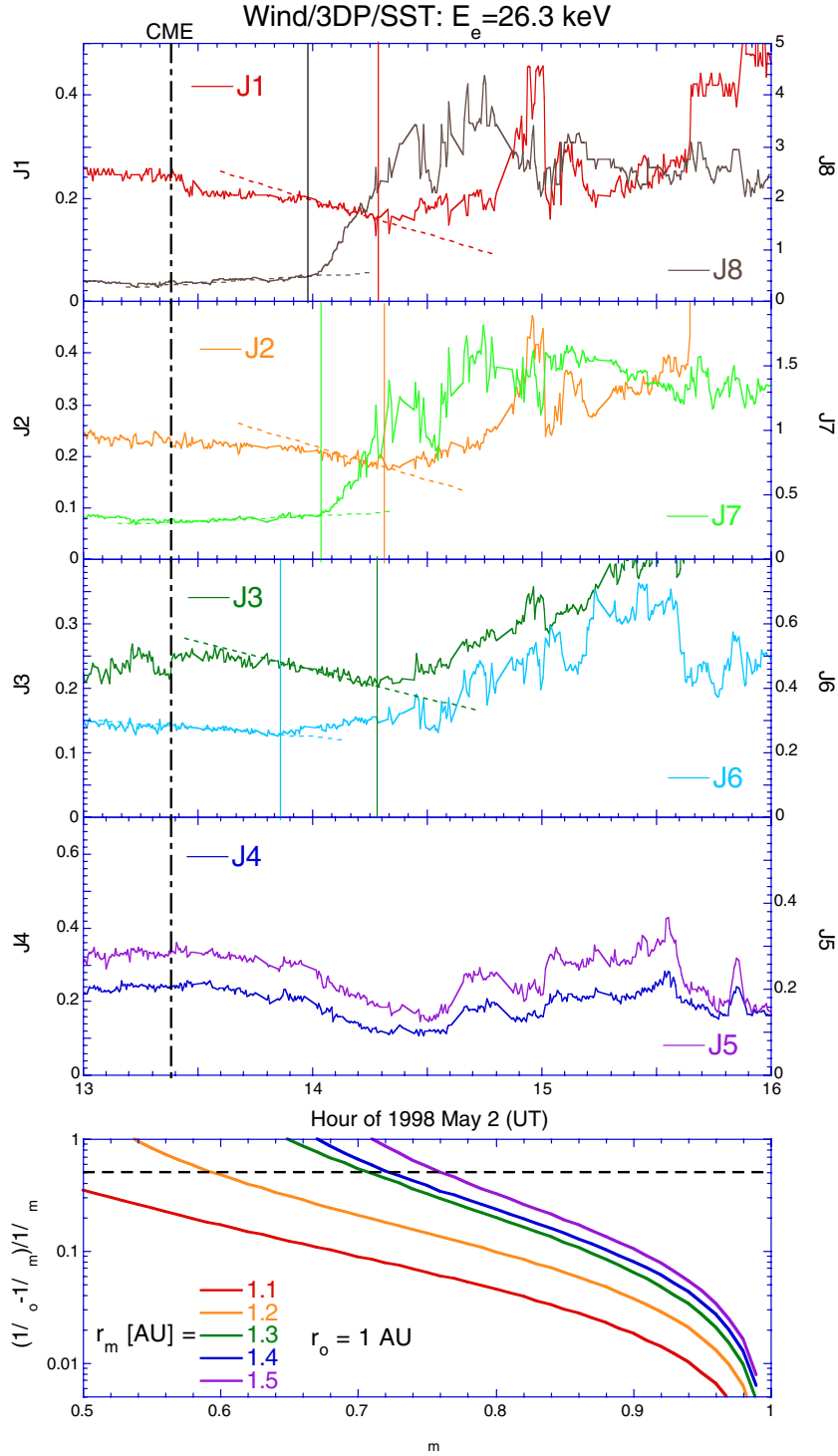$$r_t^2/r^2 = (1 - \mu^2)/(1 - \mu_t^2). \qquad (11)$$

Figure 12. Time profiles of directional electron intensities in the matched μ channels (i.e., with the same $|\mu|$ value) of incident and reflected electrons are shown for the lowest energy channel ($E_e = 26.3$ keV) of the SST sensor in the 1998 May 2 event. Also, from the Parker model (Equation (3)) the $1/\mu$ value ($1/\mu_m$) of particles at r_m is compared with that ($1/\mu_o$) at $r_o = 1$ AU in the bottom panel.

(A color version of this figure is available in the online journal.)

At the mirroring point $r = r_m$ we have $\mu_m = 0$, so $r_m = r_t \sqrt{(1 - \mu_t^2)}$, and Equation (10) becomes

$$\int_{r_m}^{r_t} dl/\mu v \sim (v \langle \cos\theta_{sB}\rangle)^{-1} \int_{r_t \sqrt{1-\mu_t^2}}^{r_t} r\,dr\left(r^2 - \left(1 - \mu_t^2\right)r_t^2\right)^{-1/2}$$

$$\sim (r_t/\langle\cos\theta_{sB}\rangle)\mu_t/v. \qquad (12)$$

Since $\mu_t \sim \mu_o$ (see above), from Equation (7) we have

$$\Delta t \sim (r_t/\langle\cos\theta_{sB}\rangle)\mu_o/v + l_{to}/(\mu_o v)$$

$$\sim (r_t/\langle\cos\theta_{sB}\rangle)(\mu_o/v)\left(1 + (\langle\cos\theta_{sB}\rangle\, l_{to}/r_t)\mu_o^{-2}\right)$$

$$\sim (r_t/\langle\cos\theta_{sB}\rangle)\left(1 + k\,\mu_o^{-2}\right)(\mu_o/v), \qquad (13)$$
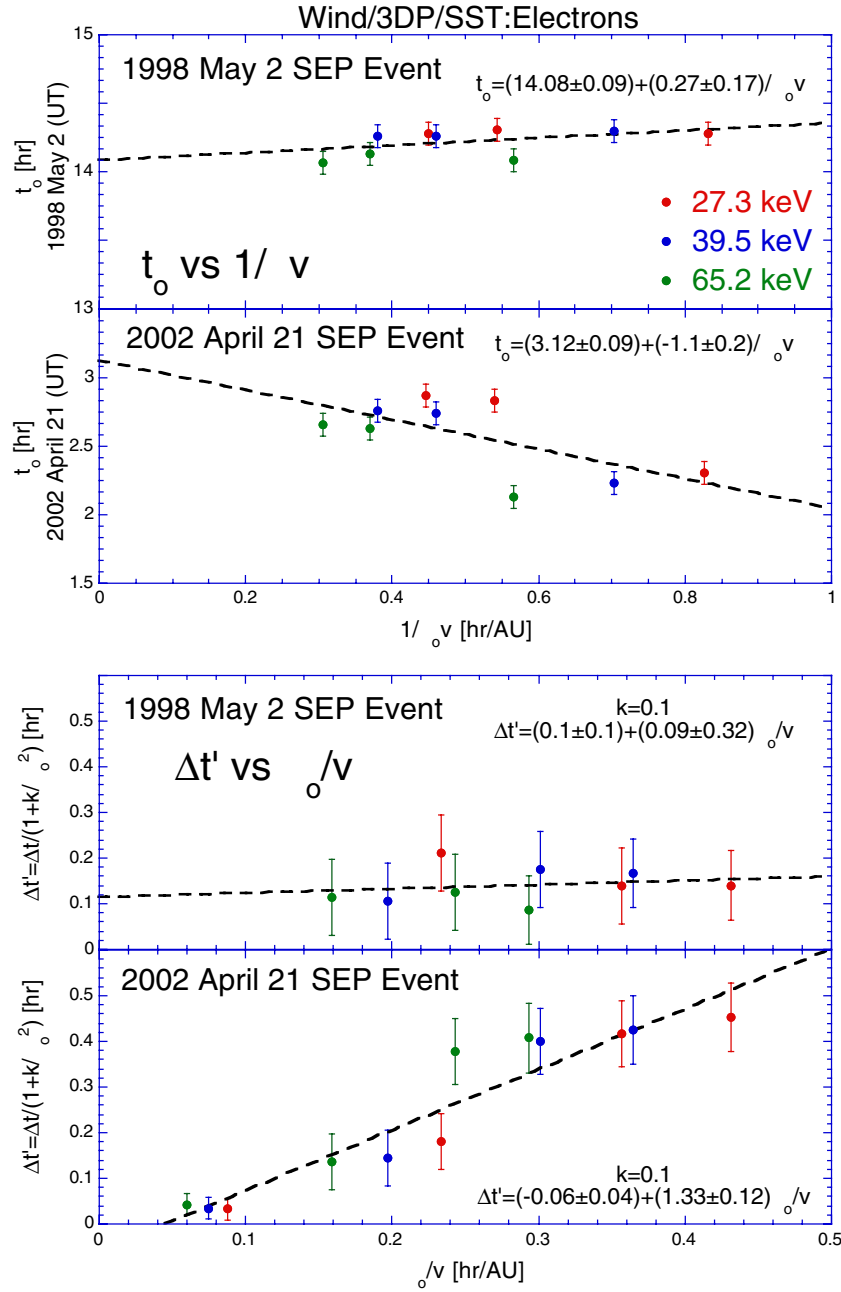
Figure 13. Arrival time t_o of reflected particles is plotted vs. $1/\mu_o v$, where μ_o is μ value observed at 1 AU, in the 1998 May 2 event (top panel) and the 2002 April 21 event (second panel). Also, the corrected traveling time interval of reflected particles from their reflecting point to 1 AU, $\Delta t' = \Delta t/(1 + k\mu_o^{-2})$ (see the text), is plotted vs. μ_o/v in the 1998 May 2 event (third panel) and the 2002 April 21 event (bottom panel) at $k = 0.1$.

(A color version of this figure is available in the online journal.)

where $k = \langle\cos(\theta_{sB})\rangle l_{to}/r_t$. Thus,

$$\Delta t' = \Delta t/\left(1 + k\,\mu_o^{-2}\right) \sim (r_t/\langle\cos\theta_{sB}\rangle)(\mu_o/v). \quad (14)$$

Note that on the right-hand side of Equation (14) μ_o is in the numerator, whereas in Equation (6) μ_o is in the denominator. This difference of μ_o location is important, because only Equation (14) indicates that reflected particles with smaller μ_o value could arrive at the 1 AU observer earlier, which is consistent with our observation in the April event shown in Figure 14.

We hence estimate the intercept and slope ($r_t/\cos(\theta_{sB})$) of the fitting line for the $\Delta t'$ versus μ_o/v plot. However, since in

Equation (14) k is unknown, we first need to determine the parameter range of k, which is carried out by plotting $\Delta t'$ versus μ_o/v at different k values. The intercept, slope ($r_t/\cos(\theta_{sB})$), and linear correlation coefficient (R) thus deduced are shown in the bottom panel of Figure 14, from which it can be seen that at $k > 0.15$ the upper boundary of the error bar of the intercept begins to depart from the zero line (the horizontal dashed line). On the other hand, at $k < 0.05$ R drastically decreases with decreasing k. Thus, the green shaded region between $k = 0.05$–0.15 limits the allowable range of k, in which R shows a broad maximum and the slope ($r_t/\cos(\theta_{sB})$) is approximately k-independent. Therefore, we assume that $k = 0.10 \pm 0.05$ in further calculations. The deduced $\Delta t'$ versus μ_o/v plot is then shown in the bottom
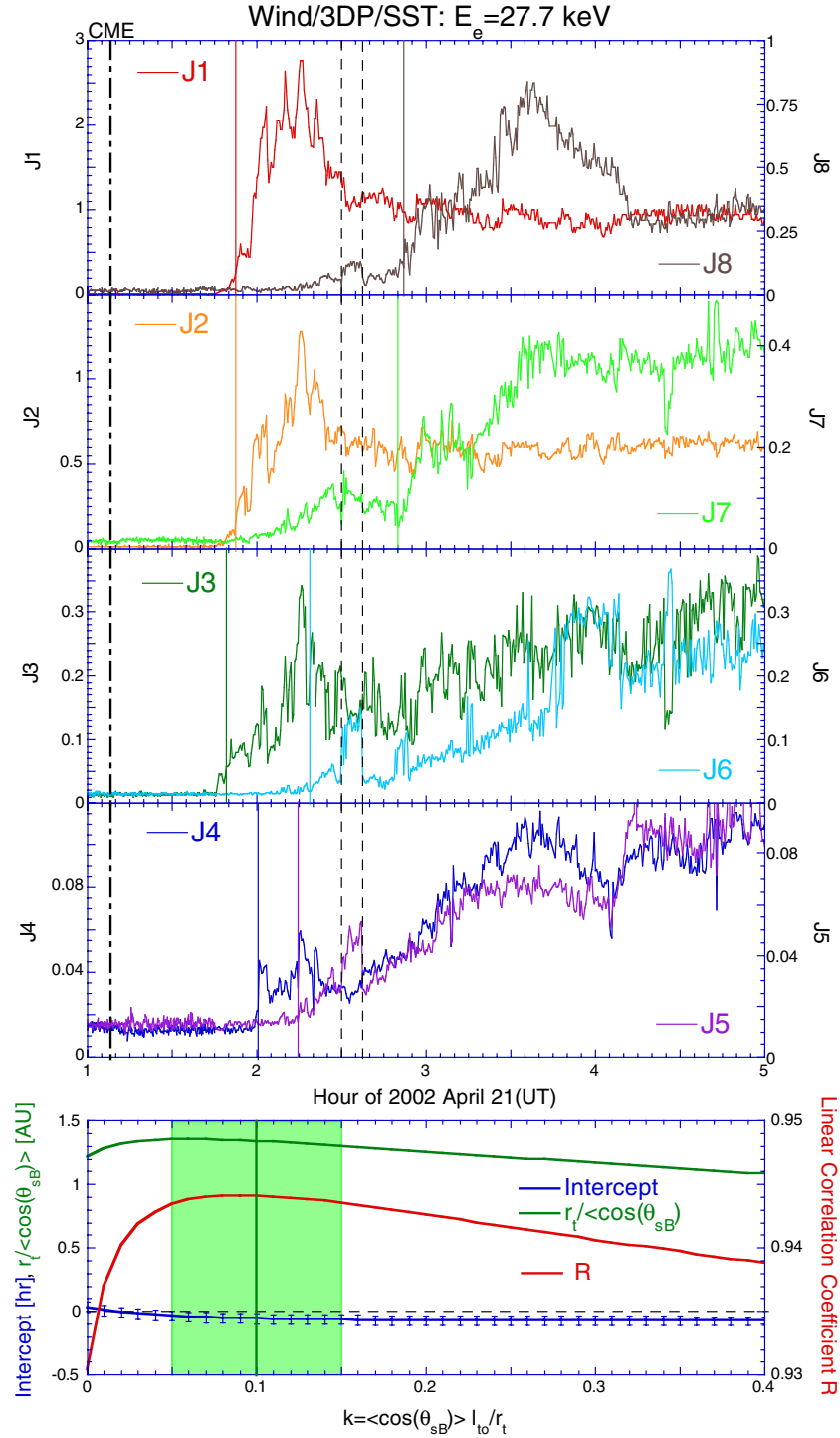
Figure 14. Same as Figure 12, but for the lowest energy channel ($E_e = 27.7$ keV) of the SST sensor in the 2002 April 21 event, where the two vertical dashed lines limit the interval of interfering electrons. Also, the intercept, slope ($r_t/\cos(\theta_{sB})$), and linear correlation coefficient (R) of the corrected traveling time interval $\Delta t'$ vs. μ_o/v plot are shown as a function of k (see the text) in the bottom panel, where the green shaded region indicates the k range constrained by observations.
(A color version of this figure is available in the online journal.)

panel of Figure 13, which exhibits that the intercept of the fitting straight line is close to zero. Further, from the deduced slope ($r_t/\langle\cos\theta_{sB}\rangle$) = 1.33 ± 0.12 AU we obtain $r_t = 1.17 \pm 0.20$ AU and $l_{st} = 1.34 \pm 0.23$ AU under the condition of $V_{sw} \sim 500$ km s^{-1}. Also, from $k = 0.10 \pm 0.05$ we find $l_{to} = 0.13 \pm 0.07$ AU. Thus, the total length of the field line between the Sun and the 1 AU observer is $l_{so} = l_{st} + l_{to} = 1.47 \pm 0.24$ AU, which is the path length of reflected particles with $\mu \sim -1$.

Therefore, in Table 2 l_{so} is explained as l_{mo} given for $\mu \sim -1$ reflected electrons. It can be seen that l_{so} is consistent with the path length (1.3 ± 0.7 AU; see Table 2) of $\mu \sim -1$ reflected electrons deduced from the L_0 difference between reflected and incident electrons. However, the calculation accuracy of l_{so} from the PAD analysis is significantly higher than that from the L_0 difference. Therefore, the PAD observation confirms that in the April event the MC has a magnetic bottle topology.

In order to test the consistency of our analysis, we also plot $\Delta t'$ versus μ_{o}/v for the May event in the third panel of Figure 13, from which we note that the May event is inconsistent with Equation (14) because of the deduced slope $(r_{\mathrm{t}}/\langle\cos\theta_{\mathrm{sB}}\rangle)$ being much less than 1 AU.

6.3. Can Perpendicular Diffusion of Particles Cause Counter-streaming Particle Beams?

Recently, Qin et al. (2011) claimed that in the 2001 September 24 event examined by Tan et al. (2009) the appearance of a counter-streaming particle beam with a strong $90°$ pitch-angle depression could be simulated by the perpendicular diffusion of particles from adjacent field lines. They assumed a large perpendicular diffusion coefficient at large distance that allows distant particle entry onto the observed field line and produces a counter-streaming particle beam. In their simulation, the parallel ($\lambda_{\parallel}$) and perpendicular ($\lambda_{\perp}$) mean free paths of $\sim$40 keV electrons are assumed to be $\sim$0.3 AU and $\sim$0.03 AU, respectively.

However, it should be emphasized that the diffusive transport scenario with $\lambda_{\parallel}\sim0.3$ AU of $\sim$40 keV electrons as assumed in the simulation of Qin et al. (2011) is inconsistent with the observational and theoretical evidences given in Tan et al. (2011). In fact, within the *Wind*/3DP/SST measured energy range (25–500 keV) Tan et al. (2011) found the existence of an electron energy window, across which the scatter-free transport of lower energy electrons would change to the diffusive transport of higher energy electrons. While the window location is SEP event-dependent, the observational evidence clearly displays that in the September event the transport of $\sim$40 keV electrons is scatter-free.

In addition, even if we preserve the diffusive transport assumption of $\sim$40 keV electrons as in Qin et al. (2011), we should note that flare-related particles are much fewer than shock-accelerated particles because of the small acceleration site in the parent flare of particles. Also, beyond the spacecraft orbit a large fraction of particles that diffuse perpendicularly from postulated flare particle population at $>45°$ away in longitude would continue to stream outward. As a result, only a very small number of sunward-traveling particles may originate from their parent flare.

In fact, the simulation result shown in Figure 3 of Qin et al. (2011) does not exhibit a particle depression at $\mu\sim0$ as observed by Tan et al. (2009), contrary to their claim.

7. SUMMARY

In this work, we have carried out a thorough analysis of two large SEP events that occurred inside MCs during the solar cycle 23: the 1998 May 2 and 2002 April 21 events.

1. The PAD properties of non-relativistic electrons measured by the *Wind*/3DP/SST and EESA-H sensors in the two events examined clearly display the presence of a reflected electron beam. However, the details of the reflected electron distributions are different. In the May event the peak intensity of the reflected electrons is located at $\mu_{\mathrm{po}}\sim$ 0.7–0.8 as observed at 1 AU, while in the April event $\mu_{\mathrm{po}}\sim-1$.

2. Comparison of the path length traveled by incident non-relativistic electrons with that by $\sim$MeV nucleon^{-1} He ions in similar time intervals indicates the stability of magnetic loop structure during a period of a few hours.

3. The joint analysis of PADs and peak intensities of electrons exhibits that in the April event the reflected particles with $\mu_{\mathrm{po}}\sim-1$ as observed at 1 AU could reach the vicinity of the Sun, implying that the magnetic loop is a magnetic bottle connected to the Sun with its two legs. In contrast, in the May event particle reflection occurs abruptly at the magnetic mirror formed by a compressed field enhancement behind an IP shock, consistent with its open field line topology.

4. The so-called reservoir effect that the presence of a reflecting boundary could enhance the duration of high-energy proton intensities is consistent with our observations. The relatively shorter duration of high-energy proton intensities in the May event is probably due to an additional escape of the protons inside the loss cone of the PAD.

APPENDIX

ANGULAR RESPONSE OF *WIND*/3DP DETECTORS

Below we analyze the angular response of *Wind*/3DP EESA-H and SST detectors in some details. The geometric factor $\Delta S_0\Delta\Omega_0$, where ΔS_0 and $\Delta\Omega_0$ are the area and solid angle elements, respectively, of different 3DP detectors, is listed in Table 1 of Lin et al. (1995). Note that the use of $\Delta\Omega_0$ only provides a very rough description of the detector's angular response, because it assumes that the response function of each element (pixel) is a δ-function (see below). However, the real response function is a continuous function. As shown in the bottom panel of Figure 6 in Lin et al. (1995), the response function of each EESA-H pixel in longitude (ϕ) can be approximated by a Gaussian function with an FWHM of $\sim8°$.

Therefore, during the data reduction process of 3DP detectors there are two window functions that may play a role: (1) a longitudinal window $\Delta\phi$ to scan a pixel forming an angular bin. For EESA-H the angular bins near the ecliptic plane have $\Delta\phi=22°.5$, while the angular bins near the poles have $\Delta\phi=45°$ or $90°$. This makes each angular bin covering a solid angle of approximately the same size ($\sim22°.5\times22°.5$). For SST the angular bin is $\sim22°.5\times36°$. (2) A pitch angle window with $\Delta\alpha=22°.5$ to sample all angular bins inside a pitch angle sector. Since the FWHM of a pixel is much less than that of an angular bin, the effect of the pixel width is negligible. Therefore, below we only examine the effect of the pitch angle window.

The transformation from the response function of an angular bin (the objective function B) to the PAD (the image function A) is realized by using the 1D convolution (e.g., Castleman 1996),

$$A(t)=\int B(\tau)\,W(t,\,\tau)\,d\tau, \qquad (A1)$$

where W is the window function. The discrete form of the 1D convolution is

$$A(i) = \sum_{i'} B(i')W_i(i - i'), \tag{A2}$$

where the window function is defined as

$$W_i(i - i') = 1 \quad \text{when} \quad i_{wLT} \leqslant (i - i') \leqslant i_{wUT}$$
$$W_i(i - i') = 0 \quad \text{when} \quad (i - i') < i_{wLT} \text{ or } (i - i') > i_{wUT}, \tag{A3}$$

where i_{wLT} and i_{wUT} are the locations of the lower and upper boundaries of the window, respectively.

Here we first estimate the objective function $B(i')$, which is the contribution of an angular bin, whose center is located at any possible position between i_{wLT} and i_{wUT} along any possible orientation of the pitch angle window. Because of the variation of magnetic field orientation, the pitch angle window may sample different widths of a pitch angle bin. In addition, among different bins in EESA-H and between EESA-H and SST the bin widths are also different. We hence assume the diameter $\Delta\alpha_o = 25°$ of a circle, whose area ($\Delta\Omega_o = \pi\Delta\alpha_o{}^2/4$) is equal to the solid angle $\Delta\Omega_0 = 22°.5 \times 22°.5$, to be the 1D equivalent width of all angular bins. The relative error of angular bin widths thus caused should be less than 20%, which is the expected accuracy of our 1D convolution analysis. By assuming that all pixels, whose center is located between i_{wLT} and i_{wUT}, contribute evenly to an angular bin, we can obtain the normalized objective function $B(i')$ as shown in the top panel of Figure 15 by the dashed line.

Furthermore, with the width of $22°.5$ of the pitch-angle window, the normalized image function $A(i)$ deduced from Equation (A2) is shown in the top panel as the solid line, which is well approximated by a Gaussian function (the dotted line) with the observed standard deviation $\sigma_i = 12°.8$. Note that the Gaussian function has an important property that the convolution of two Gaussian functions produces another Gaussian function (e.g., Castleman 1996). The standard deviation of the produced image function $A(i)$ is $\sigma_i = \sqrt{(\sigma_o^2 + \sigma_w^2)}$, where σ_o and σ_w are the standard deviations of the objective function and window function, respectively. Assuming that both objective and window functions can be approximated by Gaussian functions with their FWHMs being equal to the distribution width, from $\sigma = \text{FWHM}/(2\sqrt{(2\ln2)})$ we deduce $\sigma_o = 10°.8$ and $\sigma_w = 9°.5$. Thus, the predicted $\sigma_i = \sqrt{(\sigma_o^2 + \sigma_w^2)} = 14°.4$, indicating that the relative error between the predicted and observed σ_i values is $\pm6\%$.

In Equation (A1) by assuming $B(\tau) = \delta(\tau)$, we have $A(t) = W(t, 0)$, indicating that the window width (or $\Delta\Omega_0$ in 2D) is introduced under a δ-function approximation of the objective function. Therefore, the product of the normalized image function $\varepsilon(\alpha)$ and $\Delta\Omega_0$ should express the effective solid angle fraction per unit pitch angle interval, $d\Omega/d\alpha = \varepsilon(\alpha)\Delta\Omega_0$. For sectors $I = 1 - 2$ ε_I as a function of α is shown in the second panel of Figure 15. Note that sector 1 is special because the range of ε_1 can extend to the $\alpha < 0$ region, which is in conflict with the defined range of α (between $0°$ and $180°$). Therefore, we will "fold" the ε_1 portion in the $\alpha < 0$ region to the $\alpha > 0$ region, because the data points in the $\alpha < 0$ region have also fallen into the same sector.

The contribution of each individual angular bin to the counting rate (CR) of detected electrons is

$$CR_I = \Delta S_0 \Delta\Omega_0 \int_{\alpha_L}^{\alpha_U} J_e(\alpha, \alpha_0)\varepsilon_I(\alpha)d\alpha, \tag{A4}$$

where α_0 is the characteristic angular width of the input electron intensity J_e and α_L and α_U are the lower and upper limits of integration, respectively. Note that the directional electron intensity $JI = CR_I/\Delta S_0\Delta\Omega_0$.

Further, from the SST electron data we can calculate the logarithmic increasing rate of directional electron intensity (J_e) with increasing pitch-angle cosine (μ) (Tan et al. 2011)

$$\alpha_{PAD} = d\ln(J_e)/d|\mu|. \tag{A5}$$

As explained in Tan et al. (2011), at a given particle energy channel during the entire event period of interest $\alpha_{PAD} > 3$ implies the scatter-free transport status of incident particles, whereas $\alpha_{PAD} < 1.5$ corresponds to the diffusive transport status.

From Equation (A5) the observed J_e satisfies

$$J_e \propto \exp\left(\alpha_{PAD}\mu\right). \tag{A6}$$

By expanding $\mu = \cos(\alpha) = 1 - \alpha^2/2$, we have

$$J_e \propto \exp\left(-\alpha^2/\alpha_0^2\right), \tag{A7}$$

where

$$\alpha_0 = (2/\alpha_{PAD})^{1/2}. \tag{A8}$$

Since $\alpha_{PAD} = 3$ is the lower limit of the scatter-free transport region of particles (Tan et al. 2011), the observed α_{PAD} value of ~66 keV incident electrons in the two MC events examined is between 4 and 7 (see Tan et al. 2011), which correspond to α_0 values between $40°$ and $30°$, respectively.

Below we discuss two possible applications of Equation (A4).

1. *Correlation of sectored electron intensity ratios with the size of particle-loss cones.* Since from Equation (A4) JI is the integral of $J_e(\alpha,\alpha_0)\varepsilon_I(\alpha)$ over α, we plot $j_I = J_e(\alpha,\alpha_0)\varepsilon_I(\alpha)$ at $I = 1$ and 2, as well as at different α_0 values in the lower panels of Figure 15, where we set $\alpha_U = 60°$. Note that in the presence of the loss cone (α_{loss}), in Equation (A4) α_L should be replaced by α_{loss}; thus, the directional electron intensity becomes

$$JI(\alpha_{loss}, \alpha_0) = \int_{\alpha_{loss}}^{\alpha_U} J_e(\alpha, \alpha_0)\varepsilon_I(\alpha)d\alpha. \tag{A9}$$

From j_I ($I = 1, 2$) given in Figure 15 we calculate the $JI(\alpha_{loss},\alpha_0)$ value through numerical integration. The $J1/J2$ ratio thus deduced is plotted versus α_{loss} in the bottom panel of Figure 1, from which we can estimate the α_{loss} value by using the measured $J1/J2$ data.

2. *Calculation of electron intensity difference between two adjacent sectors.* In the presence of a continuous distribution of background electrons the detection of electron intensity difference between two adjacent sectors (e.g., $J1$–$J2$ or $J8$–$J7$) can significantly reduce the background electron intensity. However, we need to prove that the intensity difference calculation does not hurt the real signal.

It can be seen from the lower panels of Figure 15 that both j_1 and j_2 exhibit broad angular distributions. However, the difference j_1–j_2 (or j_8–j_7) shows a narrower distribution with its FWHM $< 30°$. Consequently, the integration output ($J1$–$J2$ or $J8$–$J7$) from Equation (A4) can be used as a new "channel" to detect the narrow beam of electrons that could be reflected back from the vicinity of the Sun. Also, from Figure 15 it can be seen that at different α_0 values j_2 has significantly different amplitudes. However, the FWHM of j_1–j_2 is nearly invariant, indicating that the accurate form of j_2 has less effect on the angular resolution of j_1–j_2.
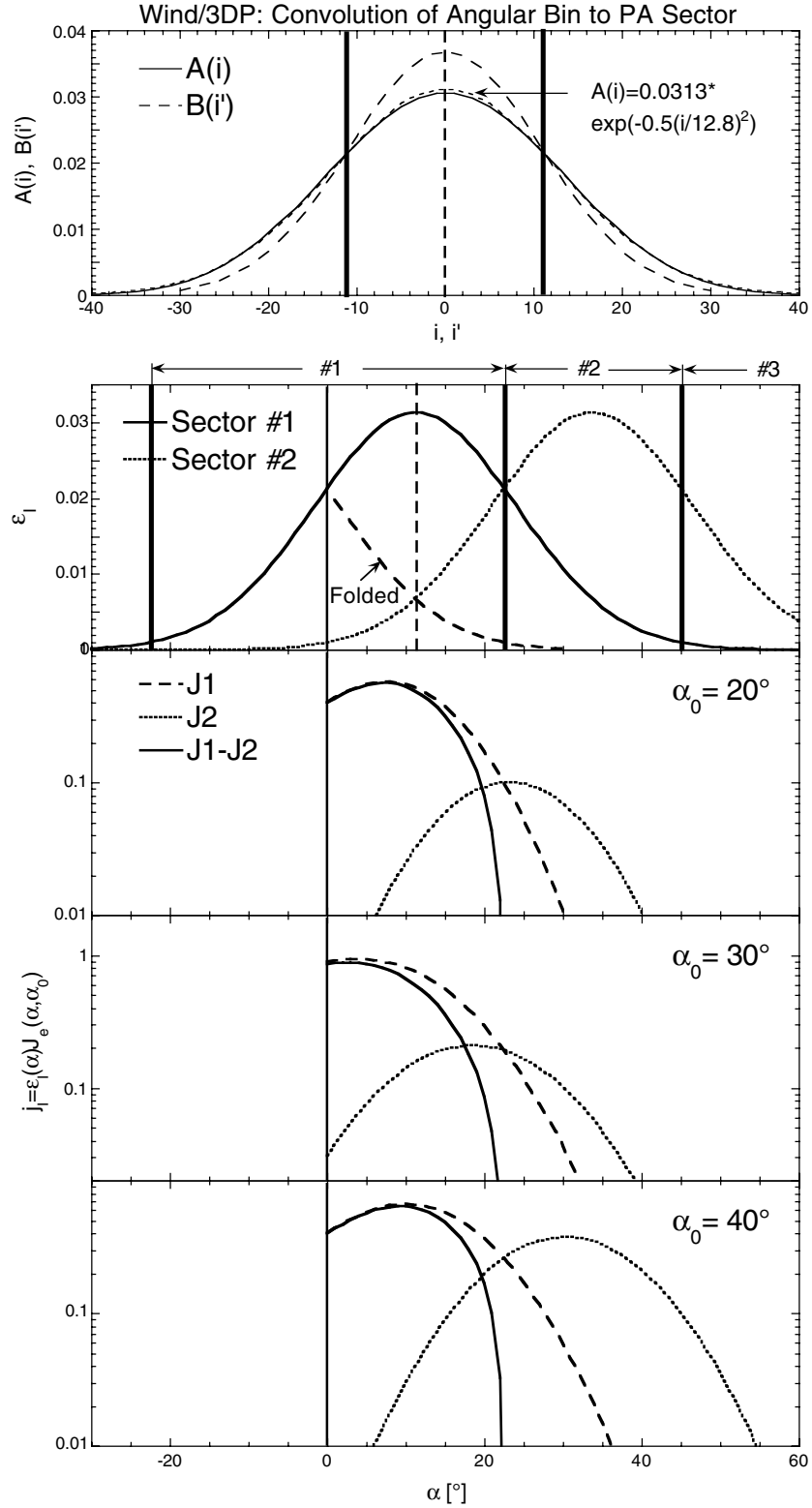
Figure 15. Top panel: the convolved result of the *Wind*/3DP angular bin to the pitch angle sector, where the dashed and solid lines are the deduced objective function and image function, respectively, and the dotted line is the Gaussian approximation of the image function. Second panel: the normalized image function $\varepsilon_I = (d\Omega/d\alpha)/\Delta\Omega_0$ of sector I ($I = 1$ or 2) (see the text) is plotted vs. the pitch angle (α) with the folded part of ε_1 denoted by the dashed line. Lower panels: $j_I = \varepsilon_I(\alpha)J_e(\alpha,\alpha_0)$, where $J_e(\alpha,\alpha_0)$ is the detected electron intensity, is plotted vs. α for different characteristic widths (α_0) of J_e.

Finally, it should be emphasized that Equation (A4) is given for a normalized image function $A(i)$, which represents the property of a single angular bin (the objective function $B(i')$).

When multiple angular bins with different $B(i')$ are grouped into the same sector, Equation (A4) can be used to estimate the average characteristics of all angular bins.

REFERENCES

Barouch, E., & Burlaga, L. F. 1976, J. Geophys. Res., 81, 2103
Berger, M. J., Seltzer, S. M., Chappell, S. E., Humphreys, J. C., & Motz, J. W. 1969, Nucl. Instrum. Methods, 69, 181
Bieber, J. W., Dröge, W., Evenson, P. A., et al. 2002, ApJ, 567, 622
Burlaga, L. F. 1988, J. Geophys. Res., 93, 7217
Burlaga, L. F., Sittler, E., Mariani, F., & Schwenn, R. 1981, J. Geophys. Res., 86, 6673
Castleman, K. R. 1996, Digital Image Processing (Englewood Cliffs, NJ: Prentice-Hall)
Dalla, S., Balogh, A., Krucker, S., et al. 2003, Ann. Geophys., 21, 1367
Gosling, J. T. 1990, in Physics of Magnetic Flux Ropes, ed. C. T. Russell (Geophysics Monograph Series 58; Washington, DC: AGU), 343
Gosling, J. T., Baker, D. N., Bame, S. J., et al. 1987, J. Geophys. Res., 92, 8519
Gosling, J. T., Skoug, R. M., & Feldman, W. C. 2001, Geophys. Rev. Lett., 28, 4155
Gosling, J. T., Skoug, R. M., & Feldman, W. C. 2002, Geophys. Rev. Lett., 29, 1573
Kahler, S. W., Haggerty, D. K., & Richardson, I. G. 2011a, ApJ, 736, 106
Kahler, S. W., Krucker, S., & Szabo, A. 2011b, J. Geophys. Res., 116, A01104
Kahler, S. W., & Reames, D. V. 1991, J. Geophys. Res., 96, 9419
Klein, L. W., & Burlaga, L. F. 1982, J. Geophys. Res., 87, 613
Klein, L. W., Burlaga, L. F., & Ness, N. F. 1987, J. Geophys. Res., 92, 9885
Kocharov, L., Laitinen, T., Al-Sawad, A., Saloniemi, E., Valtonen, E., & Reiner, M. J. 2009, ApJ, 700, L51
Kocharov, L., Saloniemi, O., Torsti, J., Kovaltsov, G., & Riihonen, E. 2007, ApJ, 654, 1121
Lario, D. 2010, ApJS, 189, 181
Larson, D. E., Lin, R. P., McTiernan, J. M., et al. 1997, Geophys. Res. Lett., 24, 1911
Lee, M. A. 2005, ApJ, 158, 38
Lin, R. P., Anderson, K. A., Ashford, S., et al. 1995, Space Sci. Rev., 71, 125
Malandraki, O. E., Sarris, E. T., & Lanzerotti, L. J. 2002, J. Atmos. Solar-Terres. Phys., 64, 517
Mann, G. 2006, in Solar Eruptions and Energetic Particles, ed. N. Gopalswamy et al. (Geophysics Monograph Series 165; Washington, DC: AGU), 221
Marsden, R. G., Sanderson, T. R., Tranquille, C., Wenzel, K.-P., & Smith, E. J. 1987, J. Geophys. Res., 92, 11009
Marubashi, K. 1986, Adv. Space Res., 6, 335
Matthaeus, W. H., Dasso, S., Weygand, J. M., Kivelson, M. G., & Osman, K. T. 2010, ApJ, 721, L10

Matthaeus, W. H., Goldstein, M. L., & Roberts, D. A. 1990, J. Geophys. Res., 95, 20673
Mewaldt, R. A., Cohen, C. M. S., Haggerty, D. K., et al. 2003, in Proc. 28th Int. Cosmic Ray Conf., Vol. 6, ed. T. Kajta, Y. Asaoka, A. Kawachi, et al. (Tokyo: Universal Academy Press), 3313
Parker, E. N. 1958, ApJ, 128, 664
Piddington, J. H. 1958, Phys. Rev., 112, 589
Qin, G., He, H.-Q., & Zhang, M. 2011, ApJ, 738, 28
Rao, U. R., McCracken, K. G., & Bukata, R. P. 1967, J. Geophys. Res., 72, 4325
Reames, D. V. 2009, ApJ, 693, 812
Reames, D. V. 2010, Solar Phys., 265, 187
Reames, D. V., Barbier, L. M., & Ng, C. K. 1996, ApJ, 466, 473
Reames, D. V., Kahler, S. W., & Tylka, A. J. 2009, ApJ, 700, L196
Reames, D. V., & Ng, C. K. 2002, ApJ, 577, L59
Richardson, I., & Cane, H. 2010, Sol. Phys., 264, 189
Roelof, E. C., Gold, R. E., Simnett, G. M., et al. 1992, Geophys. Res. Lett., 19, 1243
Ruffolo, D., Matthaeus, W. H., & Chuychai, P. 2004, ApJ, 614, 420
Shodhan, S., Crooker, N. U., Kahler, S. W., et al. 2000, J. Geophys. Res., 105, 27261
Skoug, R. M., Bame, S. J., Feldman, W. C., et al. 1999, Geophys. Res. Lett., 26, 161
Tan, L. C., Reames, D. Y., & Ng, C. K. 2008, ApJ, 678, 1471
Tan, L. C., Reames, D. V., Ng, C. K., Saloniemi, O., & Wang, L. 2009, ApJ, 701, 1753
Tan, L. C., Reames, D. V., Ng, C. K., Shao, X., & Wang, L. 2011, ApJ, 728, 133
Torsti, J., Riihonen, E., & Kocharov, L. 2004, ApJ, 600, L83
Turner, R. E. 2006, in Solar Eruptions and Energetic Particles, ed. N. Gopalswamy et al. (Geophysics Monograph Series 165; Washington, DC: AGU), 367
Tylka, A. J., Cohen, C. M. S., Dietrich, W. F., et al. 2003, in Proc. 28th Int. Cosmic Ray Conf., Vol. 6, ed. T. Kajta, Y. Asaoka, A. Kawachi, et al. (Tokyo: Universal Academy Press), 3305
Tylka, A. J., Cohen, C. M. S., Dietrich, W. F., et al. 2005, ApJ, 625, 474
Tylka, A. J., Cohen, C. M. S., Dietrich, W. F., et al. 2006, ApJS, 164, 536
Vandas, M., Odstrcil, D., & Watari, S. 2002, J. Geophys. Res., 107, 1236
von Rosenvinge, T. T., Barbier, L. M., Karsch, J., et al. 1995, Space Sci. Rev., 71, 155
Wang, L., Lin, R. P., & Krucker, S. 2011, ApJ, 727, 121
Wang, L., Lin, R. P., Krucker, S., & Gosling, J. T. 2006, Geophys. Res. Lett., 33, L03106